DEPARTMENT OF PHYSICS
UNIVERSITY OF JYVÄSKYLÄ
RESEARCH REPORT No. 5/2006

THERMAL PROPERTIES OF MESOSCOPIC WIRES AND TUNNEL JUNCTIONS

BY
LASSE TASKINEN

Academic Dissertation
for the Degree of
Doctor of Philosophy

To be presented, by permission of the
Faculty of Mathematics and Science
of the University of Jyväskylä,
for public examination in Auditorium FYS-1 of the
University of Jyväskylä on June 9, 2006
at 12 o'clock noon

Jyväskylä, Finland
June 2006

ISBN 978-951-39-3170-4

URN:ISBN:978-951-39-3170-4

Preface

The work reviewed in this thesis has been carried out during the years 1999-2006 at the Department of Physics in the University of Jyväskylä.

I would like to thank my supervisor Dr. Ilari Maasilta for the guidance during the last four years. I thank Professor Jukka Pekola for giving me the opportunity to start working in the field of the nanophysics. I have had the privilege to work with brilliant people. Especially, I wish to thank Dr. Shadyar Farhangfar, Ms. Jenni Karvonen, Dr. Jani Kivioja, Mr. Panu Koppinen, Dr. Timo Sajavaara, Dr. Marko Savolainen, Mr. Tarmo Suppula, Dr. Jussi Toppari and Mr. Maciej Zgirski for the co-operation and invaluable help. Also all the other people, with whom I have had the pleasure to work, deserve my humble acknowledgement. Excellent atmosphere in the nanophysics and SoFy groups and at the Department of Physics have made the work and the studies enjoyable.

Financial support from the Academy of Finland and Vilho, Yrjö and Kalle Väisälän rahasto are gratefully acknowledged.

Finally, I wish to thank my parents for the encouragement. Above all, I am fortunate to have my wife Sara and daughter Sanni to thank for their love and support.

Jyväskylä, May 2006

Lasse Taskinen

Abstract

Taskinen, Lasse
Thermal properties of mesoscopic wires and tunnel junctions
Jyväskylä: University of Jyväskylä, 2006, 114 p.
(Research report/Department of Physics, University of Jyväskylä,
ISSN 0075-465X; 5/2006)
ISBN 951-39-2483-1
diss.

In this thesis thermal properties of submicrometer metal wires and tunnel junctions are investigated. The emphasis is on the experimental study of electron-phonon interaction in thin metal films at sub-Kelvin temperatures. At low temperatures, the coupling between the electrons and the lattice vibrations becomes extremely small, and the electrons can be heated above the phonon temperature with a modest heating power.

Normal metal-insulator-superconductor tunnel junction pairs were utilized as a very sensitive electron thermometer, and the electron gas was heated with electric current. Measurements on power flow between electrons and phonons are presented in thin film samples of copper, gold and an alloy of aluminum and manganese (AlMn). For strongly disordered metals, the temperature dependence of the the power flow was consistent with the theory in most of the studied samples. For AlMn, electron-phonon coupling strength follows roughly linearly electron mean free path, which decreases with the increasing Mn concentration. In Cu electron mean free path increases with the film thickness, but the electron-phonon coupling does not.

An ac heating method for direct measurement of the electron-phonon energy relaxation rate is presented. Due to non-linearity of the electron-phonon coupling, the average electron temperature increases at heating frequencies comparable to the energy relaxation rate. Numerical and experimental results are presented.

Conductance of one and two dimensional arrays of tunnel junctions in weak Coulomb blockade regime were investigated at 4.2 K. Experimental results in the smallest arrays are compared with Monte Carlo simulations. The outcome was that 1D arrays suffered less from the effect of the electromagnetic environment on the tunneling than their 2D counterparts.

Keywords Electron-phonon interaction, tunneling, NIS tunnel junctions, Coulomb blockade

Author's address Lasse Taskinen
Department of Physics
Nanoscience Center
University of Jyväskylä
Finland

Supervisor Academy Researcher Dr. Ilari Maasilta
Department of Physics
Nanoscience Center
University of Jyväskylä
Finland

Reviewers Dr. Alexander Savin
Low Temperature Laboratory
Helsinki University of Technology
Finland

Dr. Dragos-Victor Anghel
Department of Theoretical Physics
National Institute of Physics and Nuclear Engineering
Romania

Opponent Dr. Joel Ullom
National Institute of Standards and Technology
Boulder, Colorado
USA

List of Publications

The main results of this thesis have been reported in the following articles:

A.I PEKOLA, J.P., TASKINEN,L.J., AND FARHANGFAR, SH, *One- and two-dimensional tunnel junction arrays in weak Coulomb blockade regime: absolute accuracy in thermometry*. Appl. Phys. Lett. **76** (1) (2000) 3747–3749.

A.II KARVONEN, J.T., TASKINEN, L.J., AND MAASILTA, I.J., *Electron-phonon interaction in thin copper and gold films*. Phys. Stat. Sol. (c) **1** (2004) 2799.

A.III TASKINEN, L.J. ,KARVONEN, J.T., AND MAASILTA, I.J., *Direct measurement of the electron-phonon relaxation rate in thin copper films*. Phys. Stat. Sol. (c) **1** (2004) 2856.

A.IV KARVONEN, J.T., TASKINEN, L.J., AND MAASILTA, I.J., *Observation of disorder-induced weakening of electron-phonon interaction in thin noble-metal films*. *Phys. Rev. B* ***72*** *(2005) 012302*.

A.V MAASILTA, I.J. AND TASKINEN, L.J., *Direct measurement of sub-Kelvin thermal relaxation rate in nanostructures*. AIP Conf. Proc. in press.

A.VI TASKINEN, L.J. ,KARVONEN, J.T., AND MAASILTA, I.J., *Electron-phonon interaction in a thin Al-Mn film*. *Nucl. Instr. and Meth. A* ***559*** *(2005) 639*.

A.VII TASKINEN, L.J. AND MAASILTA, I.J., *Electron energy relaxation by phonons in the Kondo condensate*. cond-mat/0604514, submitted for publication.

Author's contribution

The author of this thesis has written the papers A.III and A.VI and first draft of the paper A.VII. In A.I the author performed all the measurements and data analysis and made all the samples. The author has actively participated in measurements and data analysis in A.II and A.IV. The author made all the measurements and data analysis and contributed to the numerical calculations and sample fabrication in A.III. In A.V the author made all the samples and measurements. The measurements

and data analysis presented in A.VI have been done by the author. In A.VII the author was responsible for the sample fabrication, performed the numerical calculations and made all the measurements and data analysis, excluding those concerning the manganese concentration.

Contents

1 Introduction

Nowadays *nanoscience* and *nanotechnology* are often heard words even in everyday life. Nanomaterials are already used in many applications. This "Nano boom" is sustained by a multidisciplinary scientific effort made by physicists, chemists and biologist among others. The nanoscience studies the fabrication, the properties of nano-objects, and also suggest possible industrial applications. Nanotechnology, on the other hand, brings the nanodevices into the commercial world. Nanoscience finds many applications for example in semiconductor industry, where the devices have to be always faster and smaller.

This thesis is concerned with a narrow field in the more general area of condensed matter physics. The solids studied here are thin metallic films at sub-Kelvin temperatures (i.e. at temperatures less than 1K above absolute zero). The film thicknesses are of the order tens of nanometers. In this sense also this thesis belongs to the nanoscience.

The main subject studied here is *electron-phonon coupling* in thin metal films at sub-Kelvin temperatures. We try to find out how fast is the electrons relaxation process due to the interaction with the lattice vibrations (called *phonons*). At low temperatures, electron-phonon coupling is weak and the electrons can be heated to noticeably higher temperatures than the lattice. This effect is used to investigate the electron-phonon coupling. The electron temperature is measured with very sensitive normal metal-insulator-superconductor (NIS) tunnel junctions and the elecrons are Joule heated with electric current.

The effect of the electromagnetic environment on tunneling in one dimensional (1D) and two dimensional (2D) normal metal tunnel junction arrays in weak Coulomb blockade regime is studied. Such arrays can be used for thermometry at temperatures below 30 K and are called *Coulomb blockade thermometers* (CBT). The experiments on small 1D and 2D structures at 4.2 K are compared to the theoretical results. A CBT measures the electron temperature of the metal it is made of, but practical thermometry requires usually accurate measurement of the lattice temperature. Therefore, at low temperatures, the electron-phonon coupling is an important issue and has to be taken into account when designing CBT structures. It makes a connection between the two main topics of this thesis.

2 Experimental techniques

Description of the basic methods and instruments used in the sample fabrication are presented in this chapter. The feasibility of e-beam vacuum evaporation in the fabrication of thin films of an alloy of aluminum and manganese is discussed. The cryogenic apparatus and the electronics employed in the low temperature measurements are reviewed. Thermometry using normal metal-insulator-superconductor tunnel junctions plays an important role in this thesis and is introduced here.

2.1 Sample fabrication

One of the basic methods used when making submicrometer sized metallic samples is *electron beam lithography* (EBL) and *vacuum evaporation* of thin metal films [69]. The samples are usually made on silicon substrate, which has on top a thin insulating layer of silicon oxide (SiO_2) or silicon nitride (Si_3N_4). In this method, two layers of resist are spinned onto a chip and baked in between spins. The bottom layer is typically polymethylmetacrylate methacrylicacid (P(MMA/MAA)) copolymer in acetic acid and the top layer is polymethyl methacrylate (PMMA) polymer in chlorobenzene or anisol. Resists are baked on a hot plate at temperature of about 170°C for 1-15 min depending on the resist. Thickness of the top and bottom layer are typically about 400 nm and 300 nm, respectively.

Patterning of the samples takes place in a scanning electron microscope (SEM) equipped with beam blanker and patterning software. The resist from the exposed areas is removed in two step *developing* process. First developer removes resists from the exposed area. Second developer removes mainly the bottom layer, making the so-called *undercut* structure shown in Fig. 2.1.

After the development the chip is cleaned in reactive ion etcher (RIE) using oxygen plasma to get rid of all the organic residues on the exposed substrate surfaces. Then the chip is mounted onto a sample stage in the vacuum chamber of the evaporator. Deposition of the metal films studied here were performed in a *ultra high vacuum* (UHV) or Balzers electron gun evaporator with base pressures $\sim 10^{-9}$ mbar and $\sim 10^{-6}$ mbar, respectively. Sample stages in both evaporators can be rotated and tilted to change the evaporation angle.

The basic method for making tunnel junctions is depicted in Fig. 2.1. First evaporation of aluminum is done in an appropriate angle depending on the resist thick-

ness and the amount of the horizontal shift needed. After the first evaporation the chamber is pressurized with oxygen for growing a natural oxide on the surface of Al. Second evaporation of the desired metal is then done from another angle so that the two metal layers overlap.

The last step in the fabrication is the *lift-off* process. The extra resist with the metal on top of it is removed in acetone bath, the sample is rinsed in isopropanol and blown dry using Helium flow.

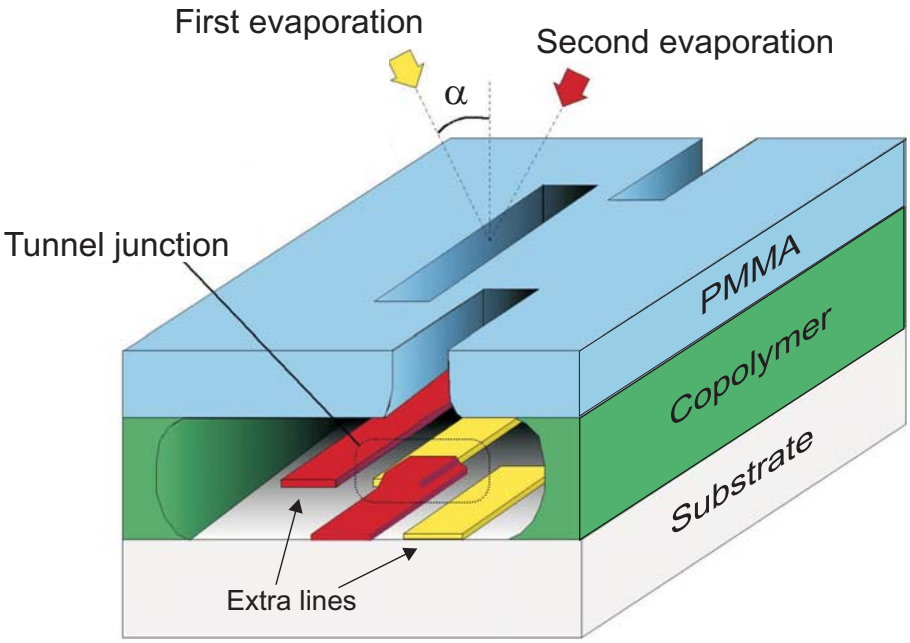

FIGURE 2.1 Shadow mask two angle evaporation method. In tunnel junctions the metal deposited first is usually Al, which is oxidised before second metal is evaporated. Evaporation angles are chosen so that the two metal layers overlap. The extra metal lines are not in contact with the tunnel junction structure.

2.1.1 Films of Aluminum doped with Manganese

One purpose of this thesis is to study properties of Aluminum manganese (AlMn) thin films made by vacuum evaporation. Since the source material is an alloy of two metals, evaporation is not straightforward. The dependence of the vapour pressures on the temperature of Al and Mn are shown in Fig. 2.2. The difference in the vapour pressures at same temperature is at least two orders of magnitude. Obvious inference is that evaporation rates of Al and Mn are quite dissimilar due to the difference in their vapour pressure. Therefore, the Mn concentration (c_i) in the evaporated film can differ from that of the source material. AlMn films were evaporated in Balzers evaporator using source material bought from Goodfellow. Source materials were Al98/Mn2 (atomic %), Al99.35/Mn0.65, and Al99.7/Mn0.3.

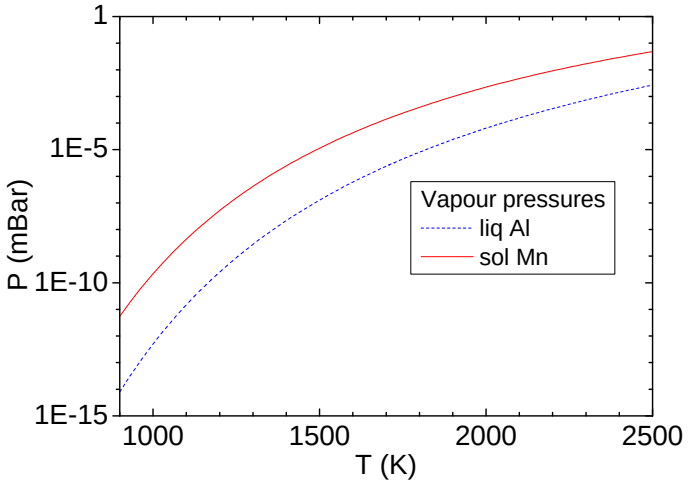

FIGURE 2.2 Vapour pressures of Aluminum and Manganese against temperature [44].

To investigate c_i in the evaporated AlMn, thin films of $\sim$ 1 cm^2 were fabricated. Mn concentration was studied using *time of flight elastic recoil detection analysis* (TOF-ERDA) set-up at the Accelerator Laboratory in the University of Helsinki. In the method, the sample to be studied is bombarded with ions and the time of the flights (TOF) of the scattered sample atoms are detected using two timing gates. An ion implanted charged particle detector is used for energy measurement of the incident sample atoms. Element is recognized from the mass, which can be calculated from the measured energy and velocity. The concentration distribution is determined from the known stopping power and scattering cross-section [55, 60].

Results of TOF-ERDA measurements on AlMn films are shown in Fig. 2.3. Also small amounts of oxygen, carbon and hydrogen are found in the film. Deduced Mn concentrations together with measured 4 K resistivities are shown in Table 2.1. The amount of manganese in the film made from the source material with 2 at. % Mn is almost six times bigger than in the source material. In the case of smaller concentrations, the Mn content has roughly doubled from the value in the source. This can probably be explained by bigger amount of source material in the crucible when evaporating from the Al98/Mn2. That had bigger lump size, and one lump in an unused crucible was always used for one evaporation. When considering different evaporations with the same source concentration, extra care was taken to keep the films as similar as possible. However, measured resistivities in several samples show that there is a moderate variation in the c_i from one evaporation to another.

Linear fit of the 4.2 K value of resistivity $\rho(0)$ versus c_i is shown in Fig. 2.4. The fit can be used for crude estimation of c_i in samples from different evaporations. The value 3.1 $\mu\Omega$cm for the resistivity at c_i = 0 was measured from an evaporated 40 nm thick Al wire at 4.2 K. The fit gives for the slope $\mathrm{d}\rho(0)/\mathrm{d}c_\mathrm{i}$ = 16 $\mu\Omega$cm/at. % and for

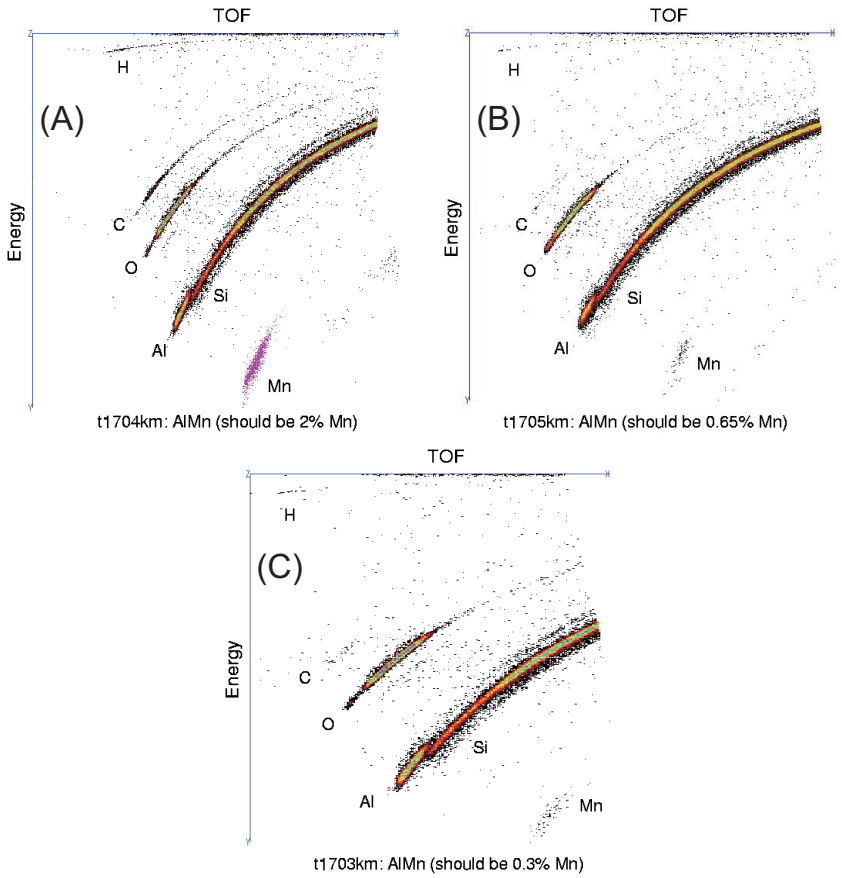

FIGURE 2.3 Measured time of flight (TOF) versus the energy of the incident atoms from TOF-ERDA measurements for the samples of Table 2.1.

the zero Mn concentration the resistivity $B = 1\ \mu\Omega\mathrm{cm}$. Result from [59] for thin dilute AlMn films prepared by sputtering ($c_\mathrm{i} < 0.3$ at. %) was $\mathrm{d}\rho(0)/\mathrm{d}c_\mathrm{i} = 13.6\ \mu\Omega\mathrm{cm}$/at. % and $B = 0.7\ \mu\Omega\mathrm{cm}$. For bulk samples with $c_\mathrm{i} > 1$ at. % earlier results [12] imply $\mathrm{d}\rho(0)/\mathrm{d}c_\mathrm{i} = 8\ \mu\Omega\mathrm{cm}$/at. % and $B = 0.07\mu\Omega\mathrm{cm}$. Different absolute values of resistivity between bulk and thin film AlMn can be at least partly explained by the shorter electron mean free path in thin films due to scattering from the film surface. Also the quality of the material can be different due to different preparation method. In any case, our results on resistivity versus Mn concentration are close to the previous studies.

TABLE 2.1 Mn concentrations c_i in the source material and in the corresponding film, and resistivity $\rho(0)$ of the film at 4.2 K

Source c_i (at. %)	Film c_i (at. %)	$\rho(0)$ ($\mu\Omega\mathrm{cm}$)
2	13.1±1	225
0.65	1.3±0.2	15.04
0.3	0.54±0.10	14.25

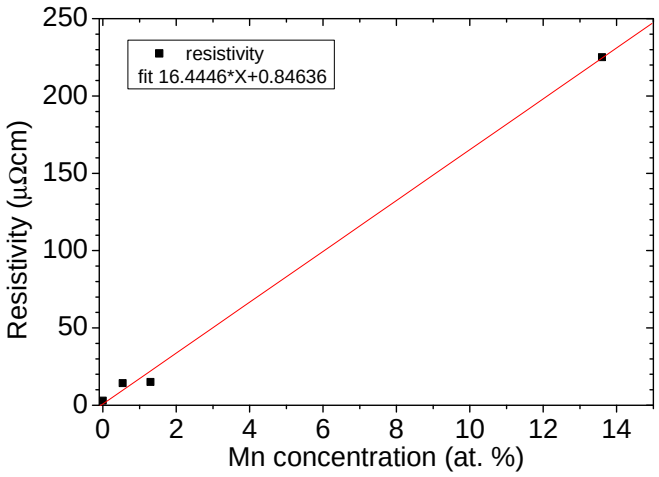

FIGURE 2.4 Squares are resistivity at 4.2 K versus Mn concentration for the samples in Table 2.1. The line is a linear fit Ax+B, with A = 16 $\mu\Omega$cm/at. % and B = 1 $\mu\Omega$cm.

2.2 Experimental details

Most of the measurements were made in a home-made plastic He^3-He^4 dilution refrigerator PDR-50 with base temperature $\sim$ 50 mK [51]. Temperature of the sample stage was measured with a calibrated Ruthenium Oxide thermometer (RuO) and Picowatt AVS-47 resistance bridge. RuO was calibrated against a Germanium resistor model GR-200A-30 from Lake Shore.

The refrigerator has ten measurement lines, as shown in Fig. 2.5. From room temperature to 4.2 K the lines are stainless steel coaxial cable type SS. Six of the lines have RC-filters at 4.2 K with nominal values are R = 1 kΩ and C = 1 μF. Two other lines have just 1 kΩ resistors at 4 K. All of these lines continue as Thermocoax down to the sample stage providing filtering for high frequencies [75]. The last two of the measurement lines continue as a twisted pair from 4 K down to sample stage for measurements where a bit higher frequencies are used (up to $\sim$ 1 MHz).

Most of the measurements were performed using low noise DL-Instrument (or Ithaco) 1211 current amplifiers and 1201 voltage amplifiers. Amplifier outputs were read using digital voltmeter (DVM) having a multiplexer input. Data was collected reading DVM through GPIB using a LabView program. Measurements took place in shielded rooms and the data was read through optical fiber to avoid galvanic connection between the measurement computer and the measurement setup in the shielded room.

In the direct electron-phonon scattering rate measurements described in Section 3.3 Agilent 33250 arbitrary waveform generator was used as the ac heating source. The generator was controlled with a LabView measurement program via GPIB.

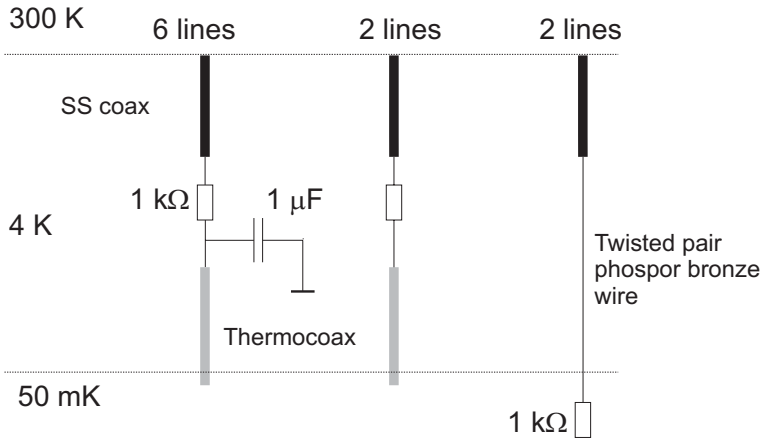

FIGURE 2.5 Measurement wiring in the PDR-50 dilution refrigerator. All lines are SS coaxial cable from room temperature to liquid helium. Six of the lines have RC-filters (R = 1 kΩ and C = 1 μF) and two have 1 kΩ resistors at liquid helium and continue as thermocoax to the sample stage. The last two lines are twisted pair down to the sample stage where there are 1 kΩ resistors.

Resistivity measurements between 300 K and 4.2 K were performed with a measurement stick which was slowly dipped into liquid helium. Temperature of the sample stage was measured with a Lake Shore Cernox CX-1070-SD-4L thermometer using Picowatt AVS-47 resistance bridge.

Measurements of tunnel junction arrays in weak Coulomb blockade regime were conducted with a 4 K measurement stick. Temperature of the helium bath was deduced by measuring the helium gas pressure by an accurate pressure gauge at the dewar pressure outlet. Measurements were conducted using Nanoway DVS-10 electronics and PC program designed for Coulomb blockade thermometry [41].

2.3 Description of tunnel junctions

Tunnel junctions discussed in this thesis consist of two metal electrodes separated by a thin oxide layer. Oxide layer is so thin that quantum mechanical tunneling through the potential barrier becomes possible. By applying a voltage V, a current I can flow through the junction. The ratio V/I defines the *tunneling resistance* R_{T}.

Electrodes of a tunnel junction can consist of normal metal (normal metal-insulator-normal metal (NIN) tunnel junction). Both electrodes can also be superconductors (SIS tunnel junction), or one electrode can be normal metal and the other superconductor (NIS tunnel junction). The SIS junctions (also known as Josephson junctions) are studied intensively for example in context with quantum computing [45]. However, in this thesis NIS and NIN tunnel junctions are more relevant. The NIN tunnel junction arrays are discussed in Chapter 5 and in attached publication [1], and the NIS tunnel junction has been used as a thermometer in most of the measurements [2,3,4,5,6,7].

For clarity, some of the basic properties of NIS tunnel junctions are reviewed here. Properties of the superconducting electrode play an important role in NIS junctions. An interested reader can find out more about superconductivity, e.g, from [70], where also NIS junctions are covered. Some basic properties needed for understanding the NIS junctions are introduced here.

In the weak coupling limit of Bardeen-Cooper-Schrieffer (BCS) theory [14], the density of quasiparticle states in the superconductor can be approximated by

$$N_S(E) = \begin{cases} N_N(0)\frac{|E|}{\sqrt{E^2-\Delta^2}} & |E| > \Delta \\ 0 & |E| < \Delta, \end{cases} \tag{2.1}$$

where E is the energy measured from the Fermi level, E_F, and Δ is the superconducting energy gap. We have assumed that the density of states (DOS) near the Fermi energy E_F in normal state is constant: $N_N(E) \approx N_N(0)$. This assumption is valid in the low temperature limit, $k_\mathrm{B}T \ll E_\mathrm{F}$. Current I through NIS junction at bias voltages V is given by the expression

$$I(V) = \frac{1}{2eR_\mathrm{T}} \int_{-\infty}^{+\infty} \mathrm{d}E\, n_\mathrm{S}(E)\left[f_\mathrm{N}(E-eV, T_\mathrm{N,e}) - f_\mathrm{N}(E+eV, T_\mathrm{N,e})\right]. \tag{2.2}$$

Here R_T is the tunneling resistance (which will be reached at large bias voltages), $n_S = N_S(E)/N_N(0)$, $T_\mathrm{N,e}$ is the electron temperature in the normal metal and f is the Fermi function $(\exp[(E-\mu)/k_\mathrm{B}T]+1)^{-1}$. As can be seen from Eq. 2.2, the current depends on the electron temperature of the normal metal, but not on the temperature of the superconductor. Hence, the NIS junction can play the role of a thermometer for the electron gas in the normal metal. At low voltages ($0 < V < \Delta/e$) and at low temperature $k_\mathrm{B}T \ll \Delta$ current depends exponentially on the voltage and temperature [47]:

$$I(V) \approx I_0 \mathrm{e}^{\frac{eV-\Delta}{k_\mathrm{B}T_\mathrm{e}}}. \tag{2.3}$$

where $I_0 = \frac{\Delta}{eR_\mathrm{T}}\sqrt{\frac{\pi k_\mathrm{B}T_\mathrm{e}}{2\Delta}}$. We observe that NIS voltage sensitivity on the normal metal temperature increases as the bias current is lowered [46]:

$$\frac{\mathrm{d}V}{\mathrm{d}T_\mathrm{e}} \approx \frac{k_\mathrm{B}}{e}\ln\left(\frac{I}{I_0}\right) \tag{2.4}$$

Another interesting feature of a NIS junction is that it can be used to cool down the electron gas in the normal metal, if the junction is biased below the energy gap ($V \leq \Delta/e$). The cooling power of NIS junction is given by

$$P_c(V) = \frac{1}{e^2R_T} \int_{-\infty}^{+\infty} \mathrm{d}E\, n_\mathrm{S}(E)[E-eV]\left[f_\mathrm{N}(E-eV, T_\mathrm{N,e}) - f_\mathrm{S}(E, T_\mathrm{S})\right]. \tag{2.5}$$

Each electron tunneling from the normal metal to the superconductor carries en-

ergy $E - eV$ with it, and dumps it into the superconductor. The NIS junctions can have cooling power of tens of picowatts and have been used even to cool down a macroscopic Germanium resistance thermometer [19].

2.4 Thermometry using SINIS structures

In the study of electron-phonon interaction, it was important to be able to measure the electron temperature of normal metal wires accurately. A very good and convenient choice for electron thermometry is normal metal-insulator-superconductor (NIS) tunnel junctions. NIS junctions can be used as a very sensitive (electron) thermometer at sub-Kelvin temperatures. Two superconducting wires connected to a normal metal through tunneling barrier forms two NIS junctions in series. This arrangement is called a SINIS structure.

The NIS junctions were fabricated by first evaporating a thin aluminum film (typical thickness 25 nm) and oxidising it thermally at room temperature with pure oxygen. Normal metal (Au, Cu or AlMn) was then evaporated on top of Al forming the other electrode of the NIS junction.

An example of a SINIS structure is shown in Fig. 2.6, which is taken with an *atomic force microscope* (AFM). The image is taken from the middle SINIS of the sample AM2 used in study the electron-phonon interaction in AlMn. The two parallel wires are made of aluminum with an oxide layer on top. AlMn wire is deposited on top of the Al and oxide.

We have used the SINIS as a thermometer by current biasing the structure and by measuring the voltage. Calibration of the thermometers were carried out by cooling (or warming) the cryostat slowly and by measuring the SINIS voltage V and the temperature of the sample stage using a RuO resistance thermometer, simultaneously. The SINIS voltage versus temperature curve obtained in such a calibration run is shown in Fig. 2.7. At temperature slightly below 200 mK, the measured SINIS voltage starts to saturate. This is due to the excess noise coming through the measurement lines. Earlier, when there were no RC filters at 4.2 K the effect was even more pronounced. This means that the electron temperature saturates to a higher value than the base temperature of the cryostat. As a consequence of this, in the heating experiment (described in Section 3.2.2), the measured V versus bath temperature curve cannot be used as the calibration curve. One has to read the correct electron temperature corresponding to the SINIS voltage from the numerically calculated BCS curve. An example of the BCS curve used for the SINIS voltage calibration is plotted in the Fig. 2.7.

The BCS calibration curve is obtained by numerically calculating Eq. 2.2 and by iterating the voltage at a given temperature to achieve the correct (bias)current used in the measurements. The energy gap Δ and the tunneling resistance R_{T} are determined by the measured current-voltage characteristics of the SINIS structure

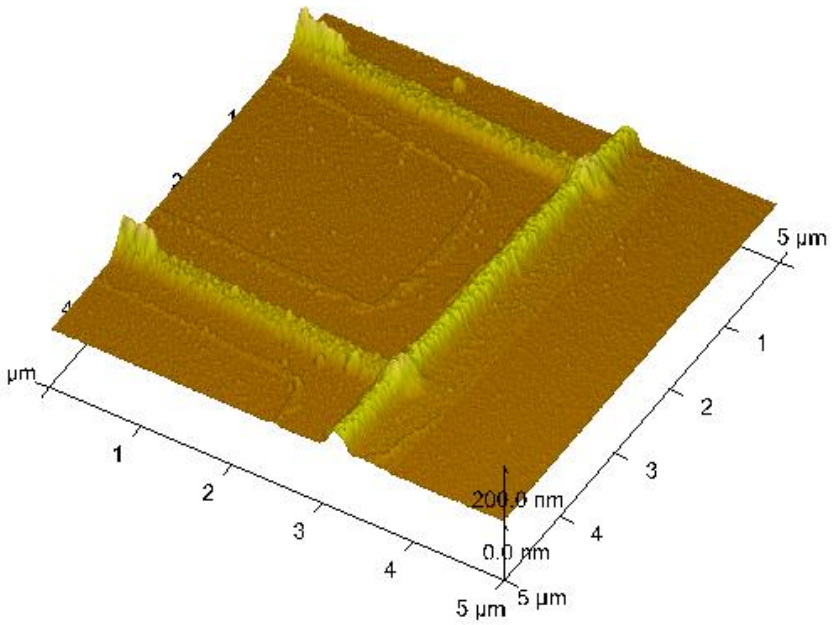

FIGURE 2.6 An atomic force microscope image of two NIS junctions. Parallel wires are Al with thermally grown oxide on top. AlMn is deposited on top of the oxide. This way two AlMn-insulator-Al tunnel junctions (SINIS structure) are formed. Al turns superconducting at temperature of about 1.5 K. Below 1 K, the SINIS structure can be used for sensitive electron thermometry of the normal metal AlMn.

at a low temperature. In the numerical calculation, the temperature dependence of the gap is also taken into account. Already above ~ 300 mK it is correct to use the measured calibration curve directly, since it gives the right electron temperature.

Fig. 2.8 shows the measured responsivity of the SINIS voltage to a small ac heating power applied to the normal metal, $\mathrm{d}V/\mathrm{d}P$, as a function of the bias current. Response of the SINIS voltage was measured with a lock-in amplifier, and the heating signal was kept as small as possible. Measurement was conducted at the cryostat base temperature of about 60 mK. Theoretically, for an ideal SINIS the responsivity should be monotonically decreasing function of I, as can be seen from Eq. 2.4 (valid when $V \leq 2\Delta$) by noting that $\mathrm{d}P \propto \mathrm{d}T_\mathrm{e}$. However, the observed responsivity has a maximum value at ~ 60 pA, which is probably due to the relative increase of leakage current at low I. This, in turn, can be understood with a finite quasiparticle DOS inside the energy gap of the superconductor [23,49].

Temperature dependence of the current-voltage characteristics of a SINIS structure can be seen in Fig. 2.9. In this sample normal metal was evaporated using

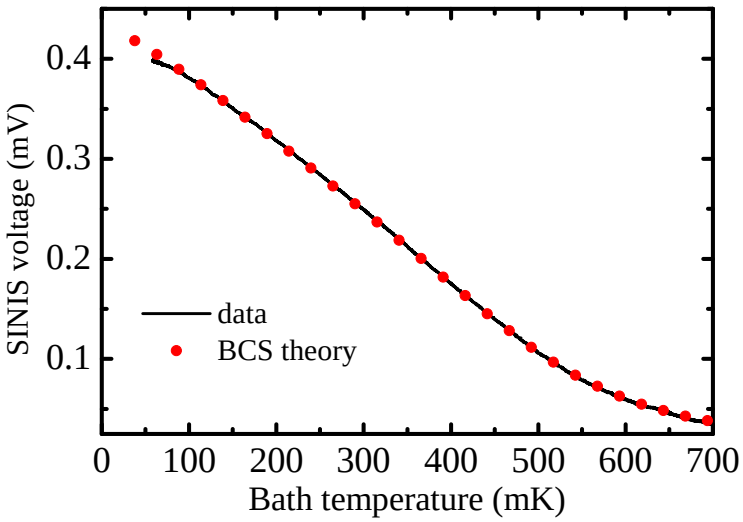

FIGURE 2.7 Typical calibration curve of the SINIS voltage versus the temperature measured at the sample stage (continuous line) and corresponding calculated BCS curve (circles).

Al99.35/Mn0.65 as a source material. Low concentration Al-Mn/Al NIS tunnel junctions have been used as thermometers before [20], and they have been shown to work like the NIS tunnel junctions with any conventional normal metal, e.g., copper.

To confirm this also for samples with higher Mn concentration, we compared the measured current-voltage curves with numerical calculations. In calculating current-voltage characteristics, we used the thermal model introduced in [27,71,20] to obtain a good fit at the lowest temperatures.

In the thermal model for a SINIS in dynamical equilibrium, one has to solve the power equation to obtain the normal metal electron temperature:

$$-P_{\mathrm{cool}}(V) + \beta(P_{\mathrm{cool}}(V) + IV) + P_{\mathrm{s}} - P_{\mathrm{e-p}} = 0, \tag{2.6}$$

where P_{cool} is the cooling power of the SINIS, I and V are current and voltage of the SINIS, $P_{\mathrm{cool}} + IV$ is the power dissipated in the superconductor and $\beta(P_{\mathrm{cool}} + IV)$ is that part of it which flows back into the normal metal. This back-flow of energy can be due to tunneling of quasiparticles back from the superconductor. Another possibility is that phonon generated in the recombination of quasiparticles with energy 2Δ is absorbed by the normal metal [38]. $P_{\mathrm{s}} = V^2/R_s$ is dissipation due to imperfect tunnel barrier and R_s is the zero bias resistance at low temperature. The power dissipated to phonons $P_{\mathrm{e-p}}$ is calculated from Eq. 3.2 using parametrs n = 6 and Σ = 2.5×10^9 W/K^{6}m^3, obtained from the electron-phonon measurements and

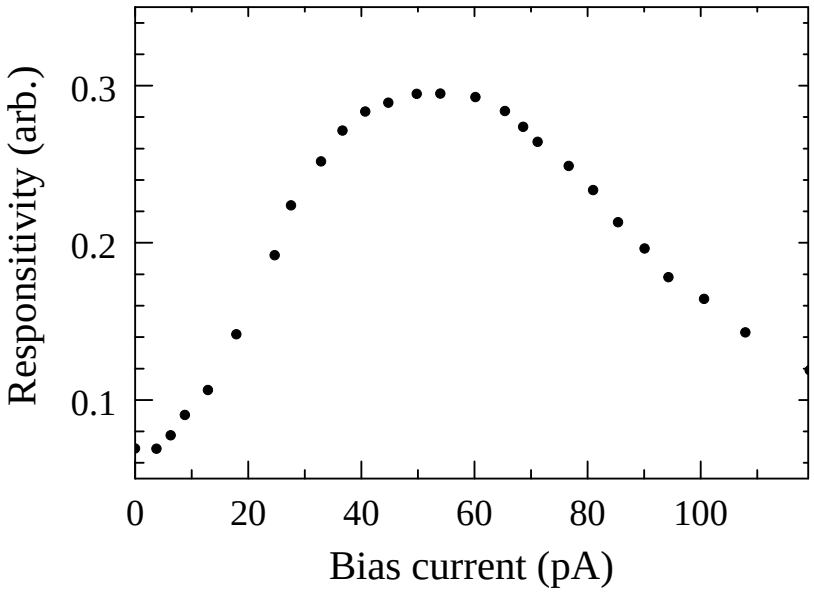

FIGURE 2.8 Measured responsivity of the SINIS voltage to a small ac heating signal applied to the normal metal ,$\mathrm{d}V/dP$, as a function of the bias current.

$\mathcal{V}$=1.1$\times$10^{-17}m^2, measured by an AFM. Cooling power of a SINIS junction can be numerically calculated using Eq. 2.5 by noting that $P_{\mathrm{cool}}(V) = 2 \times P_c(V/2)$, when assuming that the two tunnel junctions in SINIS are identical.

Although the only fitting parameter in the model is β (for the data in Fig. 2.9 β = 0.3), also the electron temperature had to be slightly adjusted; at refrigerator temperature 60 mK and at the zero bias voltage, temperature of electrons was 80 mK in the calculation. This is probably due to noise heating discussed already in the context of SINIS calibration.

Measured data in Fig. 2.9 fits to the calculated curves well. At higher voltages, calculated current-voltage curves slightly deviate from the measured ones. This can be due to simplicity of the model. For example the parameter β can be temperature dependent. The power balance equation 2.6 is practically needed only at low temperature. At temperature above $\sim$ 250 mK, the difference between pure BCS and thermal model calculations was negligible. Current-voltage characteristics of all SINIS thermometers used in this work were measured at least at the refrigerators base temperature $\sim$60 mK and found to be similar to the ones presented in Fig. 2.9. In conclusion, SINIS thermometers with AlMn as normal metal can be used as thermometer as described above.

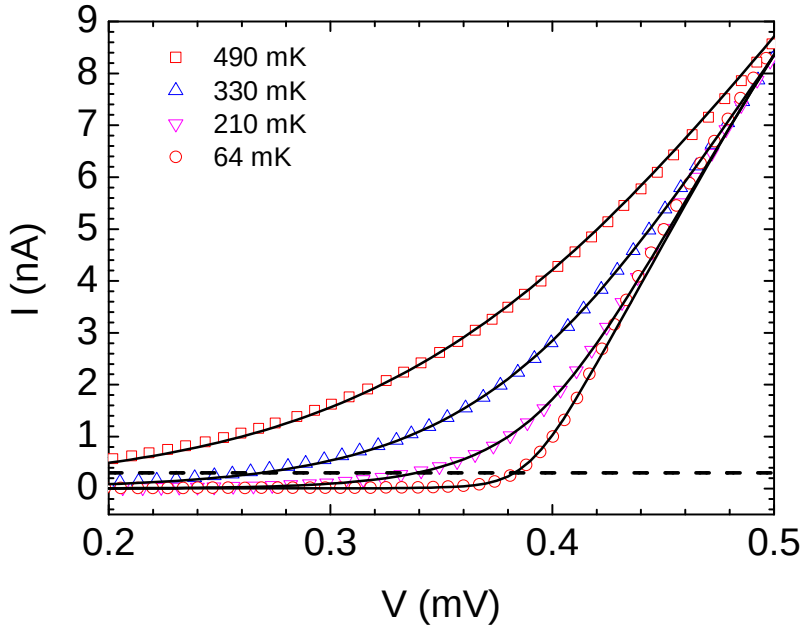

FIGURE 2.9 Current-voltage characteristics of a SINIS structure taken at different cryostat temperatures (symbols) and the theoretical curves. Dashed line indicates the value of the bias current used in the thermometry.

3 Thin noble metal films at sub-Kelvin temperatures

In this chapter experiments on electron-phonon (e-p) interaction in disordered thin gold and copper films are presented. Measurements were carried out at sub-Kelvin temperatures utilizing hot electron effect and ultrasensitive thermometry by NIS tunnel junctions. It is shown that in most of the samples the electron-phonon scattering rate follows T^4 temperature dependence, which is representative for the electron-phonon coupling mediated by vibrating disorder. The theory describing electron-phonon coupling in disordered conductors is introduced.

3.1 Theoretical background of electron-phonon interaction

The metal films studied in this thesis are thin and disordered due to the fabrication method by electron beam vacuum evaporation (see Section 2.1) and the measurements are conducted at low temperatures. Theoretical models of the electron-phonon interaction in such systems are quite well developed. The interesting thing is that the strength and temperature dependence can vary drastically depending on the level of disorder and nature of the impurities they contain. Boundaries, especially in the case of nanostructures, will affect the phenomena. Low temperatures ($T \ll \Theta_{\mathrm{D}}$, Debye temperature) makes life a bit easier by removing the need for dealing with optical phonons. Electron-phonon systems are divided into two categories with respect to parameter ql. Here q stands for the wave vector of the dominant thermal phonon and l is the mean free path of electrons. The two cases are the clean limit, when $ql > 1$, and the dirty limit, when $ql < 1$.

In Fig. 3.1 the thermal block diagram of the metal sample and the substrate is shown. The metal consists of electron subsystem and the lattice with the "local" phonons. At low temperatures, the power applied to the electron system can elevate the electron temperature T_{e} notably above the phonon temperature T_{p}, giving rise to *hot-electron effects* [58,72]. Prerequisite for these effects is that the *Kapitza resistance*, R_{K}, between metal and substrate is smaller than the thermal resistance $R_{\mathrm{e-p}}$ between the electrons and the phonons in the metal. This is usually thought to be a

fair assumption for thin films. At low enough temperature, the wavelength of thermal phonons λ_{ph} is larger than the film thickness d. Then, if the acoustic mismatch between the metal film and the substrate is small [68], the metal film cannot contain a phonon system of its own, but is tied to that of the substrate [72]. Acoustic mismatch is due to different mass densities and sound velocities in the materials.

Using a sound velocity v_{s} = 2000 m/s, the approximate phonon temperature where $\lambda_{\mathrm{ph}} \leq d = 100$ nm is $T_{\mathrm{p}} \leq hv_{\mathrm{s}}/2.82k_{\mathrm{B}}d \approx 350$ mK. However, direct experimental evidence of the magnitude of R_{K} in systems, in which one or more dimensions is small as compared to λ_{ph}, is lacking. Since $R_{\mathrm{K}} \propto 1/A$ (where A is contact area between metal film and substrate) and $R_{\mathrm{e-p}} \propto 1/Ad$, $R_{\mathrm{K}}/R_{\mathrm{e-p}} \propto d$ and R_{K} has to be taken into account at least in the case of thick films. The effect of the Kapitza resistance on the data from the electron-phonon measurements is discussed in more detail in Section 3.2.2.

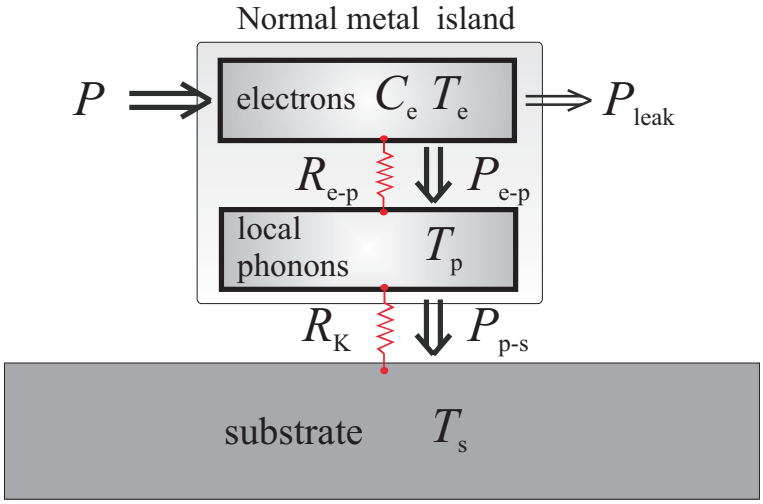

FIGURE 3.1 Thermal subsystems in metal island on substrate. P describes the power put to the electron gas. Thermal route of interest is the energy relaxation $P_{\mathrm{e-p}}$ through electron-phonon coupling denoted by thermal resistance $R_{\mathrm{e-p}}$ and $P_{\mathrm{p-s}}$ through Kapitza resistance R_{K}. Heat flow P_{leak} is the part of the heating power diffusing or radiating to measurement leads and surroundings.

Generally, the electron-phonon scattering rate between the electrons and the phonons depends strongly on temperature as

$$\tau_{e-p}^{-1} = \alpha T_{\mathrm{e}}^{m}, \tag{3.1}$$

where m can have values from 2 to 7 depending on dimensionality of the phonon system and the electron gas, plus the type and the density level of impurities and the material. This leads to the net power flow between electrons at temperature T_{e}

and phonons at temperature T_p

$$P_{e-p} = \Sigma\mathcal{V}(T_\mathrm{e}^n - T_\mathrm{p}^n), \tag{3.2}$$

where $n = m + 2$, Σ is *electron-phonon coupling constant* and $\mathcal{V}$ is the volume where the e-p interaction takes place.

The calculations for a metal in the clean limit $ql \geq 1$, with the assumption that the electrons interact only with the longitudinal (LO) phonons give $n = 5$ [28, 72]. Then the constant Σ has the expression $\Sigma \approx 0.524\alpha\gamma$ [72], where the Sommerfeld constant γ depends on the material and is related to the electronic specific heat by $C_{\mathrm{e,V}} = \gamma T_\mathrm{e}$. At low enough temperature transverse phonons need to be taken into account. In this case $n = 5$ is again obtained, but the electron-phonon relaxation rate is increased by a factor of about 15 [56].

For a metal in the dirty limit, things are a bit more complicated; one has to take into account the interference between many possible scattering mechanisms involved. Assuming an electron scattering potential, which is completely dragged by the phonons, i.e. impurities fully vibrate with the phonons (as the lattice atoms), the result is $n = 6$. Then electron-phonon coupling constant Σ is also impurity dependent. One should bear in mind that with different n, the unit of Σ is different and direct comparison between the values cannot be made.

There can be impurities or surfaces, that are not fully vibrating, e.g., "heavy" impurity atoms responsible for the scattering. Sergeev and Mitin [67] have calculated e-p scattering rate for a system containing both vibrating and static scattering potentials:

$$\frac{1}{\tau_{\mathrm{e-p}}} = \frac{3\pi^2 T^2 k_\mathrm{B}^2}{2p_\mathrm{F} l}\left(1 - \frac{\tau}{\tilde{\tau}}\right)\left(\frac{\beta_\mathrm{l}}{p_\mathrm{F}u_\mathrm{l}} + \frac{2\beta_\mathrm{t}}{p_\mathrm{F}u_\mathrm{t}}\frac{\tau}{\tilde{\tau}}\right) + \frac{\pi^4 T^4 k_\mathrm{B}^4}{5\hbar^2} p_\mathrm{F} l\left(\frac{\beta_\mathrm{l}}{(p_\mathrm{F}u_\mathrm{l})^3} + \frac{3\beta_\mathrm{t}}{(p_\mathrm{F}u_\mathrm{t})^3}\frac{\tau}{\tilde{\tau}}\right), \tag{3.3}$$

where u_l (u_t) is the longitudinal (transverse) sound velocity, l is the electron mean free path, $\beta_\mathrm{t} = \beta_\mathrm{l}(u_\mathrm{l}/u_\mathrm{t})^2 = (2\epsilon_\mathrm{F}/3)^2\nu/2\rho u_\mathrm{t}^2$, $\nu = mp_\mathrm{F}/\hbar^3\pi^2$ is the density of states at E_F, $\tau = l/v_\mathrm{F}$ is the total momentum relaxation rate, $\tilde{\tau} = \tilde{l}/v_\mathrm{F}$ is the momentum relaxation rate due to vibrating impurity potential and ρ is the mass density. If total scattering potential is due to the impurities dragged by phonons ($\tau = \tilde{\tau}$), the result will be $1/\tau_{\mathrm{e-p}} \propto T^4 l$. On the other hand, in the limit $\tilde{\tau} \to \infty$ at low temperatures, one gets $1/\tau_{\mathrm{e-p}} \propto T^2/l$, corresponding to fully static scatterers.

The equation for the power transferred from electrons to phonons calculated using scattering rates from Eq. 3.3 will naturally consist of two parts with different temperature dependence [66]:

$$\begin{aligned} P_{\mathrm{e-p}} = {} & \frac{\pi^4\nu k_\mathrm{B}^4}{5p_\mathrm{F}L}\left[\frac{\beta_\mathrm{l}}{p_\mathrm{F}u_\mathrm{l}} + \frac{2\beta_\mathrm{t}}{p_\mathrm{F}u_\mathrm{t}}\left(1 - \frac{l}{L}\right)\right]\left(T_\mathrm{e}^4 - T_\mathrm{p}^4\right) \\ & + \frac{96\pi^6\nu p_\mathrm{F} l k_\mathrm{B}^6}{925\hbar^2}\left[\frac{\beta_\mathrm{l}}{(p_\mathrm{F}u_\mathrm{l})^3} + \frac{3\beta_\mathrm{t}}{2(p_\mathrm{F}u_\mathrm{t})^3}\left(1 - \frac{l}{L}\right)\right]\left(T_\mathrm{e}^6 - T_\mathrm{p}^6\right), \end{aligned} \tag{3.4}$$

where L is now the electron mean free path due to scattering from quasistatic potential, $L = v_{\mathrm{F}}\tau_{\mathrm{qs}}$, when total momentum scattering rate is defined as $\tau = \tau_{\mathrm{qs}} + \tilde{\tau}$.

In the thermal model drawn in Fig. 3.1, the time constant for energy relaxation from the electron system at temperature T_{e} with heat capacity C_{e} connected to phonon system at T_{p} via thermal resistance $R_{\mathrm{e-p}}$ is $\tau_\epsilon = R_{\mathrm{e-p}}C_{\mathrm{e}}$. If the power flow can be depicted with Eq. 3.2, thermal resistance can be written as

$$R_{\mathrm{e-p}}^{-1} = \frac{\partial P_{\mathrm{e-p}}}{\partial T_{\mathrm{e}}} = n\Sigma\mathcal{V}T_{\mathrm{e}}^{n-1}. \tag{3.5}$$

Plugging in Eq. 3.5 and heat capacity of the electron gas $C_{\mathrm{e}} = \gamma T_{\mathrm{e}}\mathcal{V}$ one gets for the energy relaxation rate

$$\tau_\epsilon^{-1} = \frac{n\Sigma}{\gamma}T_{\mathrm{e}}^{n-2}. \tag{3.6}$$

The connection between the energy relaxation rate τ_ϵ^{-1} and the electron phonon scattering rate $\tau_{\mathrm{e-p}}^{-1}$ is [36]

$$\tau_\epsilon^{-1} = \frac{3(m+2)\Gamma(m+2)\zeta(m+2)}{2\pi^2(2-2^{-(m-1)}\Gamma(m)\zeta(m)}\,\tau_{\mathrm{e-p}}^{-1}, \tag{3.7}$$

where $\Gamma(m)$ is the gamma function, m = n - 2 and $\zeta(m)$ is the Riemann zeta function.

3.2 DC heating measurements

3.2.1 Samples

Samples were fabricated on oxidized silicon chips using standard electron beam lithography and evaporation methods as described in Section 2.1. Evaporation of the metals was done in UHV. In between evaporations of normal metal and aluminum, the sample stage was rotated 90° and tilted to large angle, $\sim$ 60°, to avoid normal and superconducting metals being in contact in other places than the junction areas. Otherwise a thick normal metal film in direct contact with superconducting Al would induce a normal state due to proximity effect.

An SEM image of a sample used for the measurements in the study of electron-phonon interaction in Cu and Au is shown in Fig. 3.2 (a) and a schematic picture is shown in Fig. 3.2 (b). The metal island, where the heat flows between the electron system and the phonon system (Section 3.2.2) is measured, is the lower long horizontal wire. The length of the wire was $l_{\mathrm{w}} \leq 500$ μm and had small variation from sample to sample. Width of the wire was typically 300-500 nm. Dimensions of the samples were measured using SEM and AFM. Sample parameters are shown in Table 3.1. The wire under investigation was connected to four superconducting Al leads. The pair of leads (going upwards from the normal metal wire) forms a SINIS

structure, which is then used as an electron thermometer. Another pair of Al leads is in direct metallic contact with the normal metal wire, forming NS junctions. These leads are used to heat the sample. Another long horizontal line is also normal metal and has a pair of superconducting wires attached to it forming a SINIS. The second wire is not in direct electrical contact with the lower wire.

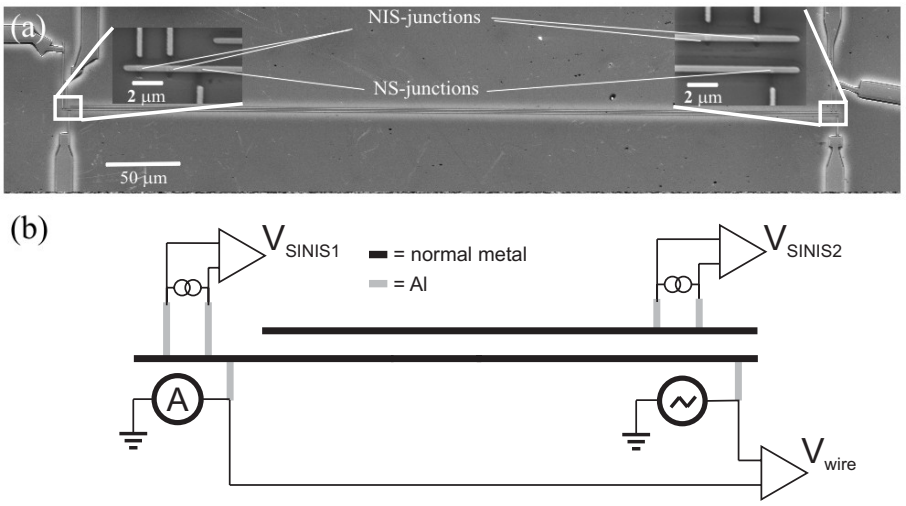

FIGURE 3.2 (a) An SEM image of a sample. Long horizontal lines are normal metal. Closer look on the SN and NIS junction areas are shown in the insets. (b) Schematic of the sample and the measurement circuit. Normal metal is heated with dc current and the electron temperature is measured with SINIS thermometers. Power injected to the electron gas of the normal metal is deduced by measuring the voltage and the current through the wire by four probe setup.

3.2.2 Measurement scheme and results

To investigate the power flow between electrons and phonons, the electron gas of the normal metal film was Joule heated by a *slowly* ramped current through the SN junctions, while the electron temperature of the wire was measured with the SINIS thermometer. The power $P = VI$ injected to the electron gas of the normal metal was calculated from the measured current I through and voltage V across the normal metal wire. The measurement circuit is depicted in the Fig. 3.2 (b).

Applicability of the measurement scheme is based on the following facts:

(*i*) Heat leak through the SN junctions is much smaller than the heat flow from electrons in the normal metal to the phonons. Clean SN junctions provide excellent electrical, but poor thermal conductivity due to Andreev reflection, as long as SN junctions are biased within the superconducting gap Δ of Al. This is the case in all the data shown here, since the resistance of the SN junctions was found to be much lower than that of the normal metal wires used in the measurements.

(*ii*) Heat conduction through the NIS junctions was also estimated. Calculations showed that small temperature gradient in the wire will develop, but it is fractions of mK and does not affect the results.

(*iii*) Third possible route for energy transfer is photon emission [63], but it is also estimated to be insignificant due to the "large" volume of the normal metal wire. An estimation for the critical temperature below which the photon heat conductivity would exceed $R_{\mathrm{e-p}}^{-1}$ in the smallest volumes we have used is about 40 mK, using $\Sigma = 2 \times 10^{10}$ W/m^{3}K^6 and 70 mK using $\Sigma = 2 \times 10^9$ W/m^{3}K^6 (n = 6). Moreover, this is for perfect match between the impedances of the electron gas and the environment, which is hardly the case.

(*iv*) Electron-electron (*e-e*) scattering length is much smaller than the length of normal metal wire and therefore electrons in the wire have well-defined Fermi distribution [54]. Distortion of the electron distribution function due to multiple Andreev reflections [52] should also be negligible in the long normal metal wires used in these measurements.

Based on the arguments (*i*)-(*iii*), we can say that electron-phonon coupling is the dominant way by which the electron gas in the normal metal wire reduces its energy. Using the notations of Fig. 3.1, we can write $P = P_{\mathrm{e-p}} = P_{\mathrm{p-s}}$. This is assumed from now on in this thesis. Point (*iv*) ensures that the electron gas has a well-defined temperature T_{e}. Since the heated wire is rather homogeous, the injected Joule power will heat the wire uniformly.

Another question is, whether the Kapitza resistance R_{K} between metal film and the substrate affects the analysis or not. A qualitative picture can be drawn by assuming some finite value for R_{K} and that the power P injected into the electron gas relaxes through the $R_{\mathrm{e-p}}$ and R_{K} to the substrate which is at temperature T_{S}. Power flow via phonons through an interface between the metal and the substrate (see Fig. 3.1) is of the form $P_{\mathrm{p-s}} = \sigma A(T_{\mathrm{p}}^4 - T_{\mathrm{s}}^4)$ [68], where A is contact area between metal film and the substrate and σ is material dependent parameter. In this case the phonon temperature of the metal wire is given by

$$T_{\mathrm{p}} = \left(\frac{P}{\sigma A} + T_{\mathrm{S}} \right)^{1/4}. \tag{3.8}$$

Combining this with Eq. 3.2 in case n = 6 yields

$$T_{\mathrm{e}} = \left[\frac{P}{\Sigma \mathcal{V}} + \left(\frac{P}{\sigma A} + T_{\mathrm{S}} \right)^{3/2} \right]^{1/6}. \tag{3.9}$$

This has been plotted for film thickess d = 30 nm, 90 nm and 150 nm at substrate temperature 60 mK in Fig. 3.3. Values for the parameters are: Σ = 2$\times 10^{10}$ W/K^{6}m^3,

σ = 280W/K^{4}m^2 (value between Cu and quartz from [68]) and $A = 1.5 \times 10^{-10}$m^2. The continuous line is the expected result for zero R_{K} if $T_{\mathrm{p}} \ll T_{\mathrm{e}}$ and we use the approximation

$$T_{\mathrm{e}} \approx (P/\Sigma\mathcal{V})^{1/n} \tag{3.10}$$

with n = 6 in the figure. As expected, the thicker the film the bigger the deviation from Eq. 3.10. Also the value of Σ influences the outcome. Smaller Σ will naturally push result of Eq. 3.9 closer to that of Eq. 3.10.

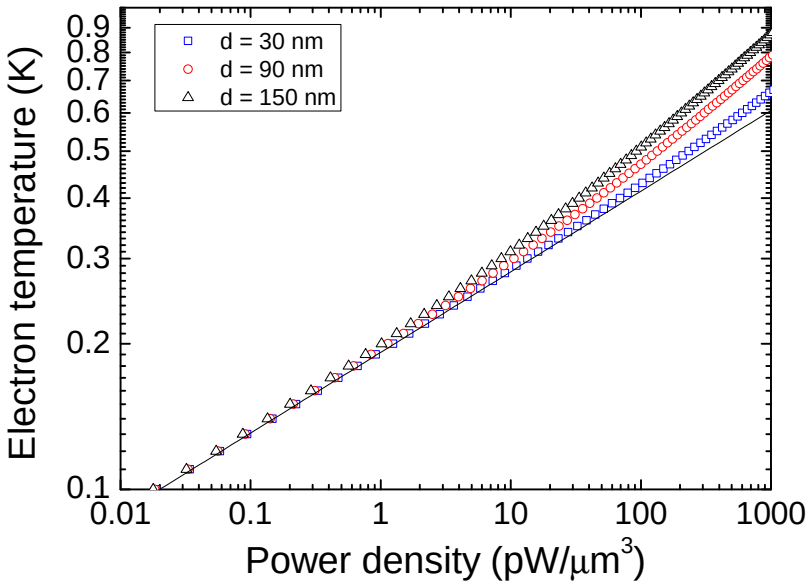

FIGURE 3.3 Calculated electron temperatures as a function of heating power density using Eq. 3.9. Film thickness in the calculation was d = 30 nm (squares), d = 90 nm (circles) and d = 150 nm (triangles). Other parameters were Σ = 2×10^{10} W/K^{6}m^3, σ = 280 W/K^{4}m^2 and $A = 1.5 \times 10^{-10}$m^2.

Samples with Cu as the normal metal with three film thicknesses and one sample with Au were measured. The measured electron temperatures in the heated wires of the samples versus the power density injected to the normal metal are shown in Fig. 3.4. Analyzing the data without knowing T_{p} can be justified to some extent by measuring the electron temperature on the reference wire, which is the upper long horizontal wire in Fig. 3.2. This gives a rough estimate for the phonon temperature in the substrate close to the heated wire.

Possible Kapitza resistance between the metal film and the substrate would make the observed power n smaller as shown in Fig. 3.3. This is not seen in the data, except maybe for the thickest sample. On the other hand, the electrons in the reference wire could be heated directly by heat transfer via photons between the two wires. In this case, and if R_{K} was negligible, an upper limit for the T_{p} in the heated

wire can be given.

An example of simultaneously measured electron temperatures versus injected power density on the heated and reference wires in sample CU33 are shown in Fig. 3.5. Measurements show that electron temperature on the other wire stays low enough so that $T_{\mathrm{p}}^n \ll T_{\mathrm{e}}^n$ in relevant heating power range for all samples, and one can use the approximation made in Eq. 3.10. In this case, the slope on the log-log plot of the measured T_{e} vs. P gives directly the value $1/n$, whereas Σ is obtained by one parameter fit to Eq. 3.10 when the volume $\mathcal{V}$ is known.

The dependence of the T_{e} on the heating power in the samples Au57, CU33 and CU84 is close to $P^{1/6}$, which is consistent with the theory for disordered film in the dirty limit $ql < 1$, provided that scattering from the fully vibrating impurities dominates. The thickest film, i.e. sample CU140, shows a behaviour of T_{e} on P which is $P^{1/5}$ at least on the high temperature end.

In Cu samples the dependence of Σ on the mean free path l of electrons is opposite to the one expected from the theory, if electron-phonon scattering was due to vibrating impurities. Σ seems to decrease with increasing l. As can be seen from Eq. 3.4, $\Sigma \propto 1/l$ in the case where the scattering is due to static impurities. However, in this case n should be 4, which is clearly not the case.

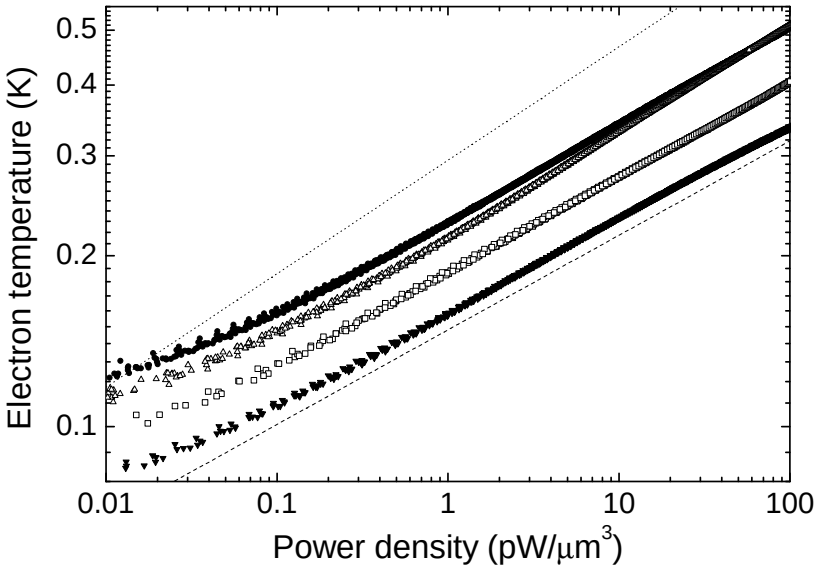

FIGURE 3.4 Measured electron temperature as a function of power density injected to the electron gas from copper and gold samples: CU33 (open square), CU84 (circle), CU140 (open triangle), and AU57 (triangle). Dashed and dotted lines are guides for eye of the type $T_{\mathrm{e}} \propto P^{1/5}$ and $T_{\mathrm{e}} \propto P^{1/6}$, respectively.

For a closer look on the exponent n, the logarithmic derivative $d(\log T_{\mathrm{e}})/d(\log P)$ for the data shown in Fig. 3.4 is presented in Fig.3.6. Though the derivatives are a bit

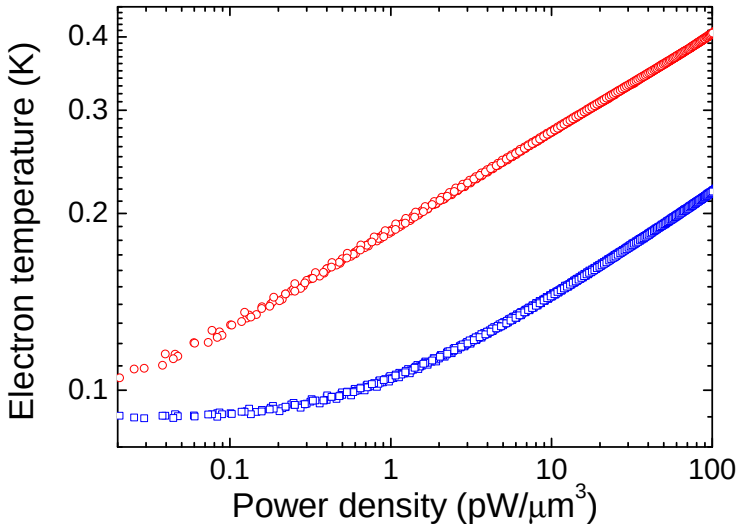

FIGURE 3.5 Measured electron temperatures versus power density in the heated wire (circles) and in the reference wire (squares) in the sample CU33.

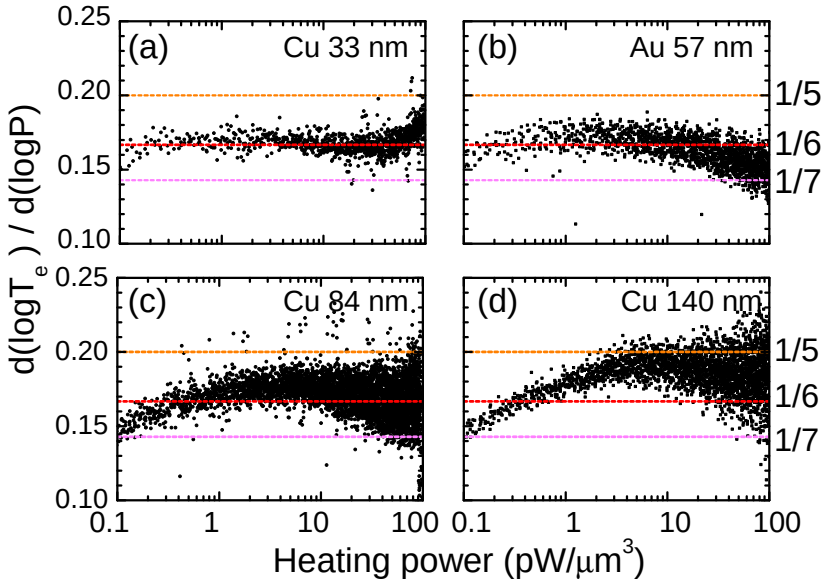

FIGURE 3.6 Numerical logarithmic derivatives $\mathrm{d}(\log T_\mathrm{e})/\mathrm{d}(\log P)$ of the data of Fig. 3.4: CU33 (a), AU57 (b), CU84 (c), and CU140 (D). Dashed lines correspond to 1/5, 1/6, and 1/7 from top down, respectively.

noisy, $n = 6$ is clearly most consistent with samples CU33 and AU57. Derivative of the data for CU84 raises a bit over $n = 6$, but is still closer to 6 than 5. Data for CU140 approaches the $n = 5$ line without clear plateau. In light of these data, $n = 6$ is con-

sistent with the data in most of the measurement range, except for the 140 nm thick Copper film in sample CU140, despite the fact that also this sample should be in the limit $ql < 1$. Possible explanations to this exists. First of all, there can be more static impurities involved in the electron-phonon scattering, which would change the qualitative behaviour. Another explanation is, that this is the effect of the Kapitza resistance. As was shown in Fig. 3.3, the thicker the film, the stronger the influence of R_{K} on n obtained from the measurements. As a result not too much value can be given to the data for the CU140 result.

TABLE 3.1 Sample parameters. l is mean free path of electrons, d is normal metal film thickness, n is the exponent in Eq. 3.10 and Σ is electron-phonon coupling constant.

Sample	Normal metal	d (nm)	l (nm)	n	Σ ($10^9 \frac{\mathrm{W}}{\mathrm{K}^n\mathrm{m}^3}$)
CU33	Cu	33	20	6	22
CU84	Cu	84	42	6	6.3
CU140	Cu	140	61	5	2.5
AU57	Au	57	24	6	60

3.3 Direct measurement of energy relaxation rate

In this measurement scheme, an alternating voltage $V_{\mathrm{heat}} = V_{\mathrm{dc}} + V_{\mathrm{ac}} \sin \omega t$ with frequency up to few MHz was used to Joule heat the electron gas of the normal metal.

Earlier, an ac heating method has been used to study electron-phonon scattering rate in thin Nb [30] and in NbC films [36]. In those studies, the amplitude of the temperature modulation in the thin films was measured. This was deduced from the frequency spectrum of the resistive response of a superconducting film biased at the middle of the superconducting transition. In addition, temperature difference between phonons and electron gas was kept small and analysis was done using linearized equation ($P_{\mathrm{e-p}} \propto T_{\mathrm{e}} - T_{\mathrm{p}}$).

Another recent development in the experimental field of nanostructure thermodynamics is a novel rf-SIN thermometer [64]. In this technique, the exponential temperature dependence of the zero bias small signal resistance R_0 of the NIS junction is used for the thermometry. At temperatures sufficiently below superconducting critical temperature T_{c},the resistance R_0 is exponentially dependent on the temperature. A NIS junction is connected to a on-chip LC resonant circuit and R_0 is deduced by measuring the power reflected from the circuit at the LC resonance frequency. With rf-SIN technique, it is possible to probe directly decay of electron temperature after fast heating pulses [65].

In the ac heating method described in this thesis, the measurement of the electron temperature T_{e} is done using sensitive SINIS thermometers. Temperature mea-

surement is performed as in the dc heating experiment by current biasing the SINIS structure and measuring the dc voltage. First version of the method was introduced in [42]. Due to the non-linearity of the electron-phonon interaction, there will be response even at dc, i.e. the average electron temperature will rise above the cut-off frequency determined by the electron-phonon scattering rate, when electron gas is heated with ac heating power. This non-linearity can be used in other thermal transport measurements in nanostructures, e.g. photon heat transfer (see. [5]).

3.3.1 Numerical calculations

The electron temperature in the presence of a heating signal $V_{\rm heat}$ can be calculated by solving the full differential equation governing the heat flow:

$$T_{\rm e}\frac{{\rm d}T_{\rm e}}{{\rm d}t} = -A(T_{\rm e}^n - T_{\rm p}^n) + P_{\rm dc} + P_\omega \sin\omega t + P_{2\omega}\cos 2\omega t, \tag{3.11}$$

where $A = \frac{\Sigma}{\gamma}$, $P_{\rm dc} = (V_{\rm dc}^2 + V_{\rm ac}^2/2)/(R\gamma\mathcal{V})$, $P_\omega = 2V_{\rm dc}V_{\rm ac}/(R\gamma\mathcal{V})$ and $P_{2\omega} = V_{\rm ac}^2/(2R\gamma\mathcal{V})$. Here Σ is the electron-phonon coupling constant, $\mathcal{V}$ is the sample volume, γ is the Sommerfeld constant and R is resistance of the heated wire. Since Σ depends linearly on γ, the temperature relaxation rate does not depend on the heat capacity and is only dependent on the electron-phonon scattering rate.

Eq. 3.11 was solved numerically for exponents n = 5 and 6, corresponding to $1/\tau_{\rm e-p} = \alpha T_{\rm e}^{n-2}$. From the $T_{\rm e}(t)$ curve, the steady state average electron temperature $T_{\rm e}(\omega)$ has been determined as a function of ω. Calculations were done with realistic sample parameters. Fig. 3.7(a) shows the results obtained for two ac heating powers in the case $n = 6$ (the impure limit). As can be seen, the average $T_{\rm e}$ develops a clear step up at some cut-off frequency, and this frequency moves up as a function of $T_{\rm e}$. To be able to define this cut-off frequency unequivocally, the data is analyzed further by taking the logarithmic derivative with respect to ω. This is shown in Fig. 3.7(b). The log-derivative develops a clear peak, whose position is used as the definition of the cut-off frequency $\omega_{\rm c}$. In addition, the log-derivative shows quite clearly the effect of the strength of the non-linearity: the larger the relative ac power (top curve largest), the more non-symmetric the peak is.

In Fig. 3.8, the cut-off frequency ω_c is plotted against the low-frequency limit of electron temperature $T_{\rm e,0}$ for cases $n = 5$ and $n = 6$. It is quite clear that ω_c follows the temperature dependence expected for a cut-off determined by the electron-phonon scattering rate:

$$\omega_{\rm c} = \alpha^* T_{\rm e,0}^m, \tag{3.12}$$

where m = n-2. In addition, the coefficient α^* is close to that calculated from Equation 3.6, i.e. $\alpha^* \approx n\Sigma/\gamma$. Dashed and dotted lines in Fig. 3.8 are plotted using $\Sigma = 1.7\times10^9$ W/K^{6}m^3 for $n = 6$ and $\Sigma = 3.8 \times 10^8$ W/K^{5}m^3 for n = 5, respectively. Same values were used in the calculation of the corresponding numerical results, and lines fit to

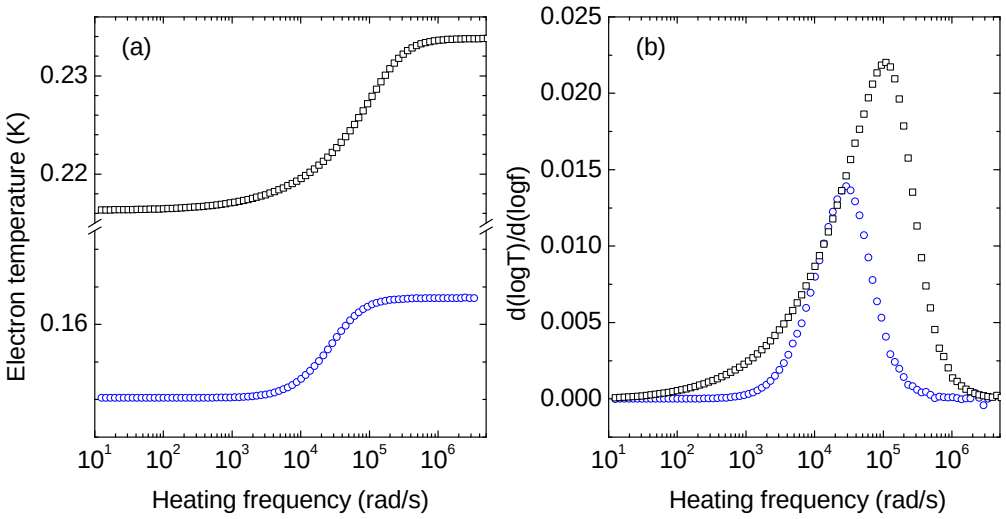

FIGURE 3.7 Calculated electron temperature versus heating frequency for two different ac heating powers (a) and corresponding logarithmic derivatives (b).

the calculated points rather well. Therefore, one can be confident that the analysis scheme outlined above will be a direct measurement of the electron-phonon scattering rate without any fitting parameters.

3.3.2 Experimental results

Samples used in these measurements were identical to those described in Section 3.2.1. The ac heating voltage was applied to the normal metal via the SN junction. The heating signal was produced with an arbitrary waveform generator. The frequency of the heating signal was changed step by step and the dc voltage of the SINIS thermometers were measured simultaneously. We took many frequency sweeps with the same ac voltage amplitude and dc voltage offset and averaged them to reduce the noise. The amplitude of the ac voltage or the dc voltage offset was then changed to obtain a different average electron temperature $T_{\mathrm{e},0}$. Naturelly one has to take into account that the actual heating frequency when V_{dc} is small as compared to the V_{ac}, is twice the frequency ω from the waveform generator.

A typical frequency sweep consisted of 300-500 frequency points between 0.1 Hz – 5 MHz. Each of the eleven representative sweeps with different ac heating power shown in Fig. 3.9 are an average of 10 frequency sweeps each. For all sweeps, overheating is clearly seen in the high frequency range between 10 kHz – 3 MHz. This can be understood by the numerical modeling discussed above.

Cut-off frequencies analyzed from the measured frequency sweeps for three samples with Cu as normal metal are shown in Fig. 3.10. Samples had film thick-

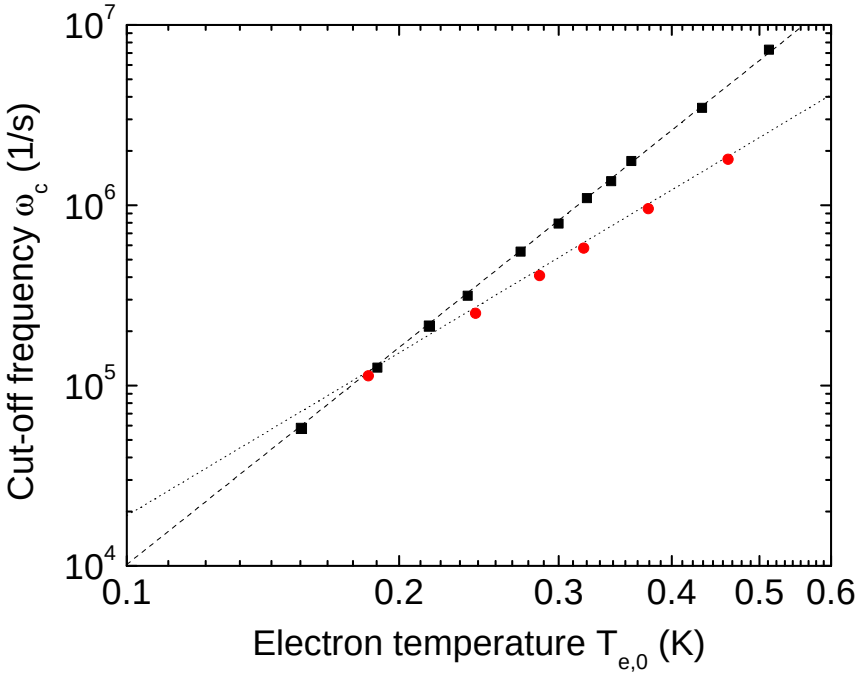

FIGURE 3.8 Cut-off frequencies deduced from the calculated $T_e(\omega)$ curves for $n = 6$ and $\Sigma = 1.7\times10^9$ W/K^{6}m^3(squares) and for $n = 5$ and $\Sigma = 3.8\times10^8$ W/K^{5}m^3(circles). Dashed line is fit with parameters $m = 4$ and α^*=1.02$\times10^9$1/sK^4 and dotted with $m = 3$ and α^*=1.82$\times10^7$1/sK^3.

nesses of 36 nm (referred to sample CU36), 41 nm (sample CU41) and 84 nm (sample CU84b). Except the unexplained low temperature fall off of the cutoff in the samples CU84b and CU41, the temperature dependence of the cut-off frequencies follows the numerical modeling. One parameter fits $\omega_c = \alpha^* T^4$ to data for the samples CU36 and CU41 gives α^* = 1.93$\times10^8$1/K^4 and α^* = 5.79$\times10^8$1/K^4, respectively. The thickest sample CU84b showed temperature dependence of ω_c expected in the clean limit ql > 1, and fit $\omega_c = \alpha \times T^3$ gave α = 2.15$\times10^7$1/K^3. Electron-phonon coupling constants deduced from these fits are shown in the Table 3.2.

TABLE 3.2 Sample parameters. d is the normal metal film thickness, m is the observed exponent as in Eq. 3.12, $n = m + 2$ and Σ is the electron-phonon coupling constant.

Sample	d (nm)	m	Σ ($10^9 \frac{\mathrm{W}}{\mathrm{K}^n\mathrm{m}^3}$)
CU36	36	4	3.1
CU41	41	4	9.4
CU84b	84	3	0.42

There are a couple of puzzling things in these results. First, there is rather large

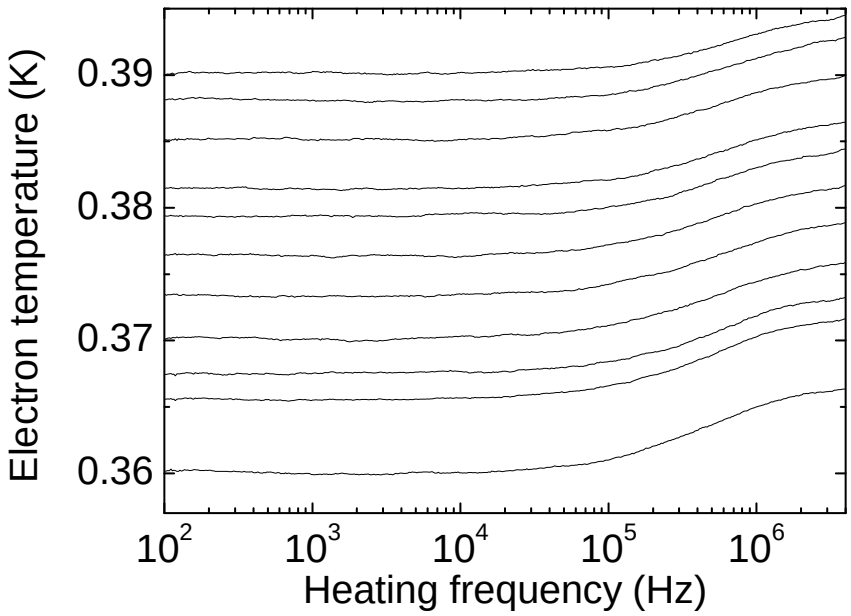

FIGURE 3.9 Electron temperature as a function of heating frequency with eleven different ac voltage amplitudes. These data are for 36 nm thick copper film.

difference between the electron-phonon coupling constants Σ for the two thinnest samples. It is natural that there would be some difference between subsequent evaporations, since Σ is sensitive to the quality of the metal film (dependence on the mean free path l). Secondly, the 84 nm thick sample showed a temperature dependence n = 5, whereas the sample CU84 in dc measurements had n = 6, or at least closer to 6 than 5. Maybe the electron mean free path l is different enough to push this sample to clean limit. This is, however, unlikely. Also the value for Σ is rather small as compared to the value for the sample CU140 with n = 5. It may be that the Kapitza resistance has large variations from sample to sample affecting the results for thickest samples. In any case, it is shown that the method introduced here offers a possibility to obtain information about the thermal relaxation rates in nanostructures.

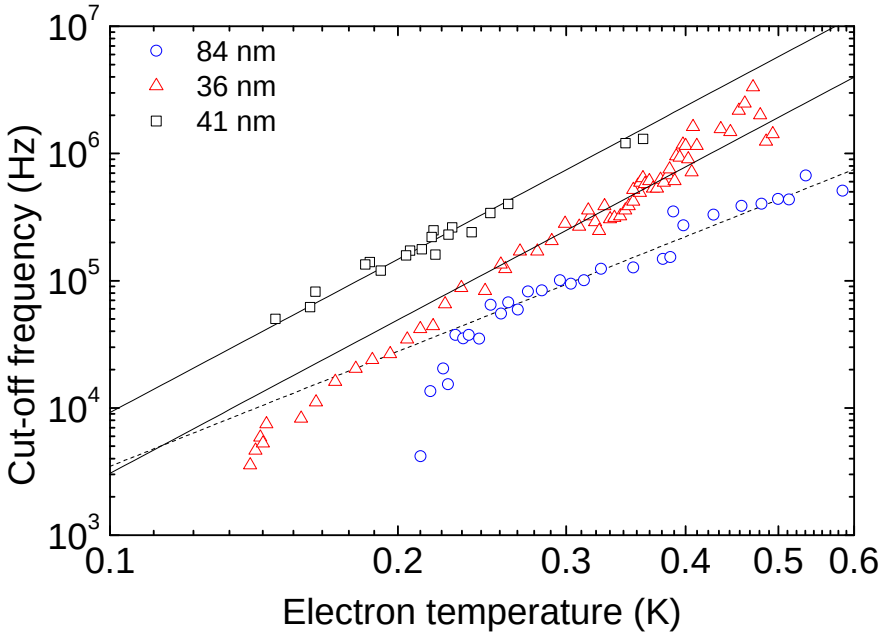

FIGURE 3.10 Cut-off frequencies obtained from the frequency sweeps for samples with 84 nm (circle), 36 nm (triangles) and 41 nm (squares) thick copper wire.

4 Aluminum Manganese thin films

The motivation for the study of an alloy of Aluminum and Manganese (AlMn) is its suitability for many low temperature applications. Superconducting transition temperature T_c of AlMn is lower than that of pure Al. In addition, tuning of T_c is moderately easy by changing the concentration of Mn [59]. Another advantage of AlMn as compared to many other metals is that it can be thermally oxidized as easily as Al and oxide forms a good insulation layer for tunnel junction applications.

AlMn has already been used in novel NIS bolometers [62], TES microcalorimeters [21] and thin-film solid-state refrigerators [20]. Electron-phonon interaction is typically the dominant energy loss channel for the electron system as a whole at low temperatures. Therefore, knowledge of the magnitude and the temperature dependence of electron-phonon interaction is very critical for the performance of bolometric detectors and solid state coolers [31]. In this chapter, an experimental study of electron-phonon interaction in thin AlMn films is presented. Since Mn is a magnetic impurity, the Kondo effect is shortly reviewed.

4.1 Kondo effect

In contrast to the constant impurity resistivity produced by the non-magnetic impurities [74], the magnetic impurities in a metal can produce a resistivity ρ_i, which increases as the temperature is lowered. As the phonon contribution to the resistivity reduces, a minimum will be found in the total resistivity. This is the phenomenon originally referred to as the *Kondo effect*. Kondo effect was observed already in the 30's, but was not explained earlier than in 1964 by Kondo [43]. Kondo managed to explain the effect by using third order perturbation theory to the so-called s-d model [32] describing the interaction between localized d-electrons and conduction s-electrons. In the model a local magnetic moment S is coupled to the conduction electrons via the exchange interaction J. Kondo showed that singular scattering of the conduction electrons near the the Fermi energy E_F together with antiferromagnetic coupling J leads to an impurity resistivity [32]

$$\rho_\mathrm{i} = \frac{3\pi m J^2 S(S+1)}{2e^2\hbar E_\mathrm{F}} \left(1 - 4J\rho_0(E_\mathrm{F}) \ln\left(\frac{k_\mathrm{B}T}{D}\right)\right), \tag{4.1}$$

where E_{F} is the Fermi energy, ρ_0 is density of states and parameter $D \gg E_{\mathrm{F}}$. However, Kondo's perturbative calculation is not valid as $T \to 0$ and the search for the full solution was named the Kondo problem.

Experimental results for the impurity resistivity ρ_{i}, e.g. for a dilute AlMn alloy show a power law $\rho_{\mathrm{i}} = \rho_0(1 - (T/\Theta)^2)$ as $T \to 0$. At a bit higher temperature, there is approximately linear region $\rho_{\mathrm{i}} = \rho_0'(1 - T/\Theta')$ and finally close to the *Kondo temperature* T_{K} a logarithmic dependence $\rho_{\mathrm{i}} = A - B \ln T$ is observed [18, 13, 12].

There is no analytical result for the whole temperature range for ρ_{i} and one has to resort to *numerical renormalization group* (NRG) approach [32]. Few points deduced from [32] calculated with NRG are plotted in Fig. 4.1 . Analytical expression for the

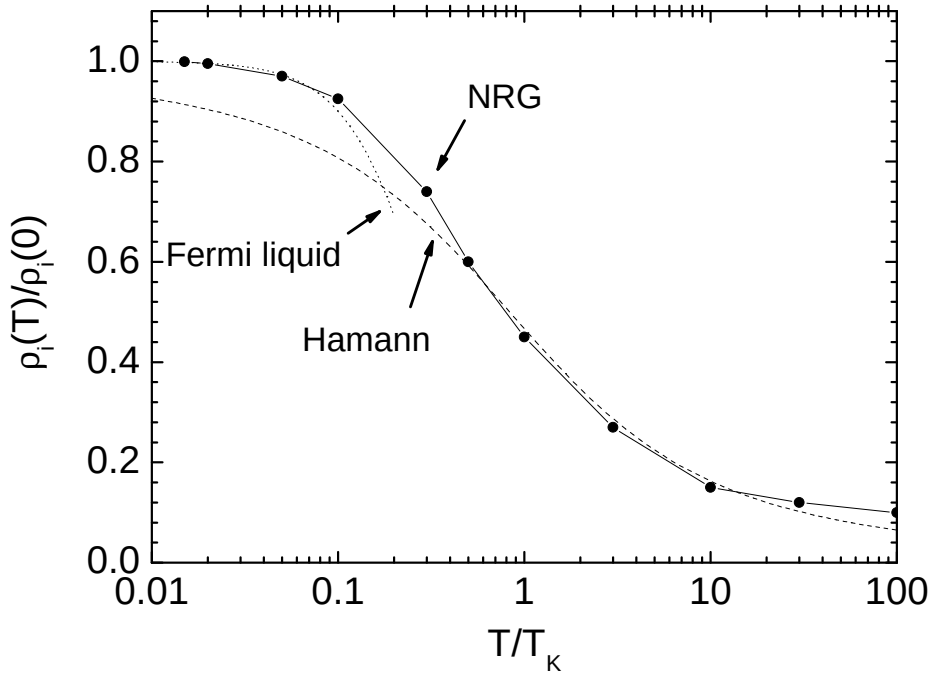

FIGURE 4.1 Normalized impurity resistivity $\rho_{\mathrm{i}}/\rho_{\mathrm{i}}(0)$ as a function of temperature calculated with numerical renormalization group approach (connected circles), Fermi liquid result (dotted line) and Hamann result (dashed line). NRG points are reproduced from [32]. Value for the spin is S=1/2.

low temperature limit can be derived using Fermi liquid theory [32]

$$\rho_{\mathrm{i}} = \rho_{\mathrm{i}}(0) \left[1 - \frac{\pi^4 w^2}{8} \left(\frac{T}{T_{\mathrm{K}}} \right)^2 \right], \tag{4.2}$$

where w = 0.4128 is the so called Wilson number. This is plotted in Fig. 4.1. In con-

trast close to T_{K} impurity resistivity is approximately [32]

$$\rho_{\mathrm{i}} = \frac{\rho_{\mathrm{i}}(0)}{2}\left[1 - \frac{\ln T/T_{\mathrm{K}}}{\left((\ln T/T_{\mathrm{K}})^2 + \pi^2 S(S+1)\right)^{1/2}}\right], \tag{4.3}$$

which is the Hamann result plotted in Fig. 4.1 with S=1/2.

Besides the temperature dependent impurity resistivity, there are also other Kondo anomalies. Magnetic susceptibility and specific heat are modified due to the interaction between conduction electrons and the magnetic impurities. Both typically increase at low temperature. For the bulk AlMn, the Sommerfeld constant varies linearly with Mn concentration and the coefficient is $\Delta\gamma/c_{\mathrm{i}}$ = 44 J/(K^{2}m^3 %) in the range c_{i} = 0.1-0.4 at. % at the temperature interval 1.4-4.2 K [57]. Sommerfeld constant for the bulk Al is γ = 135 J/K^{2}m^3. Consequently the increase in the specific heat is large at high concentrations.

Recently, lot of new understanding has emerged on how the magnetic impurities affect the dephasing [53] and energy relaxation [35, 10] of electrons at low temperatures, by a mechanism where the electron-electron (e-e) interaction is mediated by the exchange interaction with the magnetic impurities [40,29,73]. Although this new channel for the e-e interaction is clearly dominant for dephasing in most impurity-host systems, where the Kondo temperature T_K is much smaller [35, 10] or slightly higher [15] than the electron temperature, it will disappear in the limit where $T << T_K$. In this extreme unitary limit, the impurity spin is completely screened by the electrons. The electrons are scattered elastically, and Fermi-liquid theory is know to be valid, if the number of orbital channels k of the impurity equals twice the spin, $k = 2S$ [48,32].

Aluminum doped with Manganese is an impurity-host system with an extremely large Kondo temperature $T_{\mathrm{K}} \approx$ 500 K. The expected magnetic ion in this system is Mn^{2+}, and if Hund's rule applies, it has five spin aligned d-electrons, thus $k = 2S = 5$. As the Kondo impurity mediated mechanism is then suppressed at our experimental sub-Kelvin temperature range, only direct electron-electron interaction [8] and electron-phonon interaction [74] remain as the main mechanisms for electron energy loss.

4.2 Resistivity measurements

For accurate measurements of the resistivity between room temperature and 4 K, four probe samples were fabricated. These samples were made in the same evaporation runs with the films used for Manganese concentration measurements discussed in Section 2.1.1. Source materials used for the evaporation of AlMn films were Goodfellow Al98/Mn2 (atomic %) (sample RS1), Al99.35/Mn0.65 (RS2) and Al99.7/Mn0.3 (RS3). These samples had similar AlMn wire dimensions and identical evaporation parameters (growth rate, new crucible every time and same amount

of source material) than the samples used in electron-phonon interaction measurements. Area of the cross-sections of the AlMn wires for the resistivity analysis was deduced from AFM measurements.

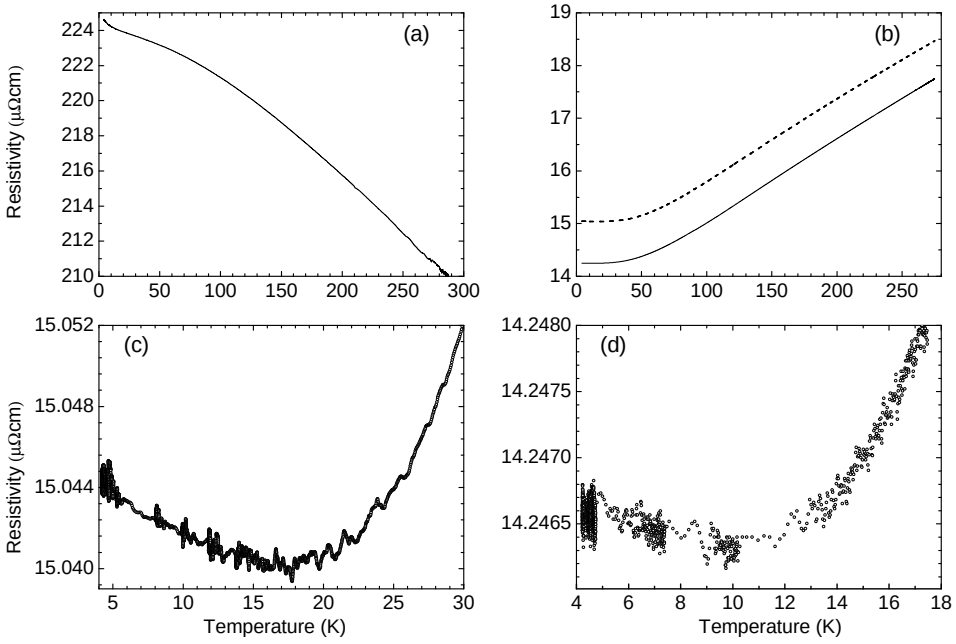

FIGURE 4.2 Measured resistivities of the AlMn four probe samples versus temperature, RS1 (a) RS2 (dotted line) and RS3 (continuous line) (b), low temperature blow up of RS2 data (c) and RS3 data (d).

Data from resistivity measurements is shown in Fig. 4.2. Samples RS2 and RS3 exhibit a typical metallic resistivity, where the phonon contribution dominates at high temperatures (region where $\mathrm{d}\rho/\mathrm{d}T > 0$), whereas below 30 K the impurity resistivity dominates. However, if one looks at the low temperature region more carefully (Figs. 4.2 (c) and (d)), clear minima for both samples can be seen. This is a signature of the Kondo effect. In sample RS1 with the highest Mn concentration, the contribution of the Kondo resistivity is so large that it completely overwhelms the phonon contribution in the whole temperature range all the way up to room temperature ($\mathrm{d}\rho/\mathrm{d}T < 0$). The shape of the ρ vs. T curve agrees qualitatively with the Kondo theory in the strong coupling limit $T < T_K$. Quantitative comparison is difficult, as the temperature range is such that only numerical renormalization group calculations are valid [32]. The residual resistivity at 4.2 K is approximately linear in c_i, as expected for the unitary limit [32].

4.3 Electron-phonon interaction measurements

Samples used in the measurements were fabricated on nitridized silicon chips using exactly the same procedure as with the Cu and Au samples. Estimated Mn concentration in the evaporated AlMn wires is shown in Table 4.1. Estimation was done using the fit shown in the Fig. 2.4.

AlMn samples had different geometry than the Cu and Au samples described in Section 3.2.1. Schematic of the samples and the measuring circuit are shown in the Fig. 4.3. Upper long horizontal line represents the heated AlMn wire. The Al lines going upwards from AlMn wire form SN junctions and the two pairs of Al lines going downwards form SINIS thermometers. The SINIS in the middle of the AlMn wire gives the electron temperature, which has to be compared with the heating power when extracting the e-p coupling information from the heating measurements data. This is due to the relatively poor heat conductivity in AlMn yielding a noticeably lower electron temperature already a few micrometers away from the part heated by the electrical current. Temperature at the end of the heated wire could be measured with the other SINIS. The other horizontal AlMn wire is the reference wire for the phonon temperature estimation. Distance between the reference wire and the heated wire is about 2 μm. There is one SINIS thermometer for the temperature measurement in the reference wire.

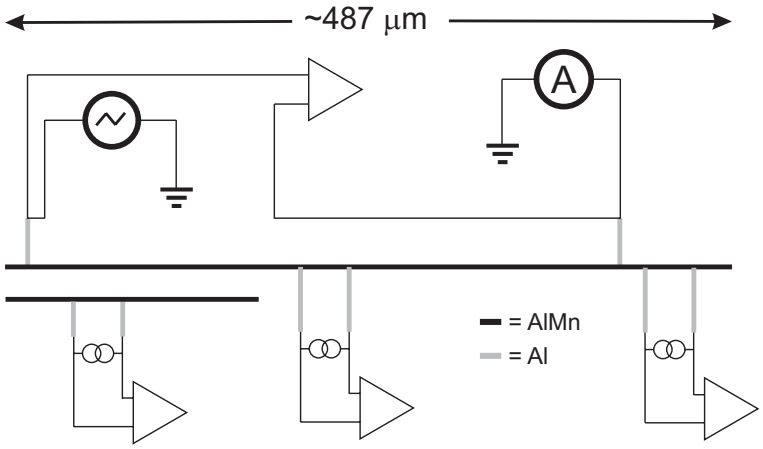

FIGURE 4.3 Schematic of the AlMn sample and the measuring circuit used for the electron-phonon measurements. Horizontal black lines denote AlMn normal metal wires and vertical grey lines are superconducting Al forming SN (lines going upwards from AlMn) and NIS (lines going downwards from AlMn) junctions with AlMn.

Results of the voltages sweeps for AlMn samples AM2, AM065 and AM03 are shown in Fig. 4.4, where the electron temperature (measured in the *middle*) in the heated wire is plotted as a function of power per unit volume of the AlMn wire, i.e. power density. It is obvious that the temperature dependence is close to $P^{1/6}$, as was the case with similar Cu and Au samples discussed in Section 3.2.2.

TABLE 4.1 Parameters of the e-p samples. c is Mn concentration in the AlMn source material. Mn concentration $c_{\rm i}$ in the sample was estimated from the measured 4 K resistivity versus Mn concentration data shown in Section 2.1.1. The mean free path l was calculated from the resistivity at $T = 60$ mK using the Drude formula, Σ was obtained from the fits to the data in Fig. 4.4. Upper limit for the ratio of the energy relaxation rates $r = (1/\tau_{\epsilon,\rm AlMn})/(1/\tau_{\epsilon,\rm Al}) = 6\Sigma T/(5\Sigma_{\rm Al})$ between AlMn and pure Al (see text for more details).

Sample	c (at. %)	$c_{\rm i}(at.\%)$	l (nm)	Σ (10^9W/K^{6}m^3)	r(0.1 K)
AM2	2	11.5	0.2	1.1	0.12
AM065	0.65	1.2	1.9	2.5	0.27
AM03	0.3	0.7	3.2	3.4	0.37

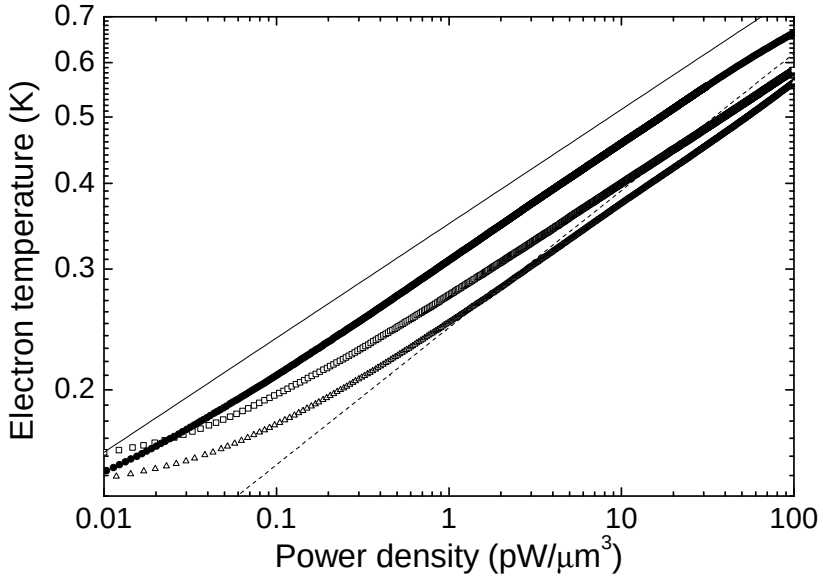

FIGURE 4.4 Measured electron temperatures versus the power density injected to the electrons from samples AM2 (circles), AM065 (square) and AM03 (star). Solid line $T_e \propto P^{1/6}$ is guide for eye. Dashed line corresponds to Al data in the pure limit, $n = 5$, with $\Sigma = 1.1 \times 10^9$ W/K^{5}m^3 calculated for sample 1 in Ref. [61], using a value for Sommerfeld constant $\gamma = 135$ J/K^{2}m^3.

One parameter fits of Eq. 3.10 to the data in Fig. 4.4 yielded values for Σ shown in Table 4.1. The trend is that in the samples with increasing Mn concentration, electron gas is less coupled to the phonons, that is, the e-p coupling constant Σ becomes smaller. This is in crude agreement with the expectation from the theory for metals in the dirty limit when the electrons are coupled to the scattering potential fully dragged by the phonons. Then Σ should be proportional to the electron mean free path l (see Eq. 3.4), which decreases with increasing Mn concentration. Electron-

phonon coupling constant as a function of the electron mean free path is plotted in Fig. 4.5.

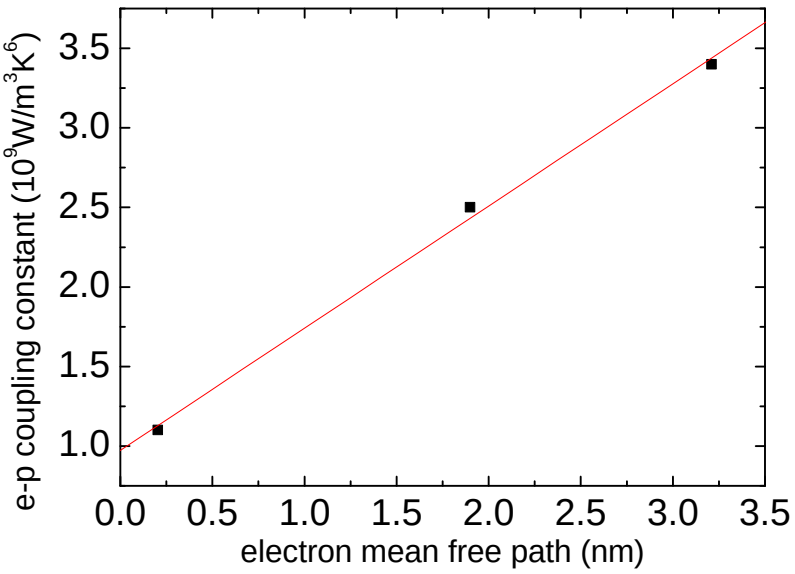

FIGURE 4.5 Electron-phonon coupling constants Σ versus the electron mean free path l from table 4.1 (squares). Line is linear fit $C + F \times l$ with C = 0.97 $\times$ 10^9 W/(m^{3}K^6) and F = 0.77 $\times$ 10^9 W/(m^{3}K^{6}nm).

The dashed line in Fig. 4.4 is the electron temperature calculated for pure Al using an e-p coupling constant $\Sigma_{\mathrm{Al}} = 1.1 \times 10^9$W/K^{5}m^3 (Eq. 3.10, n = 5). The value was calculated using a Sommerfeld constant $\gamma = 135$ J/K^{2}m^3 and data for sample 1 in Ref. [61]. Comparison of the energy relaxation rates τ_ϵ^{-1} (Eq. 3.6) of electron systems in Al and AlMn at 100 mK are also tabulated in table 4.1. The values given in the table are calculated using the same specific heat for Al and AlMn. However, the real ratio of the energy relaxation rates is $r' = (1/\tau_{AlMn})/(1/\tau_{Al}) = 6\Sigma T\gamma_{\mathrm{Al}}/(5\Sigma_{\mathrm{Al}}\gamma_{\mathrm{AlMn}})$. As discussed earlier, the specific heat increases due to magnetic impurities, so the ratios r given in the table are upper limits for real values. If increase of the Sommerfeld constant is as in the bulk AlMn, the relaxation rate suppression for AM2 is 0.03 when compared to pure Al at 100 mK. Comparison of τ_ϵ^{-1} of AlMn samples with Au and Cu samples with n = 6 yields upper limit r for the temperature independent suppression factor from 0.01 (between AM2 and Au38) to 0.8 (between AM03 and CU36), when using $\gamma = 135$ J/K^{2}m^3 for AlMn and $\gamma = 97$ J/K^{2}m^3 for Cu and Au.

To obtain more detailed picture of the dependence of T_{e} on the injected power density, plot of logarithmic derivatives $\mathrm{d}(\log T_e)/\mathrm{d}(\log P)$ of the data is presented in Fig. 4.6. Besides the drop at the beginning due to noise heating, all the samples showed n = 6 in most of the power density range. Data for AM2 consists of two

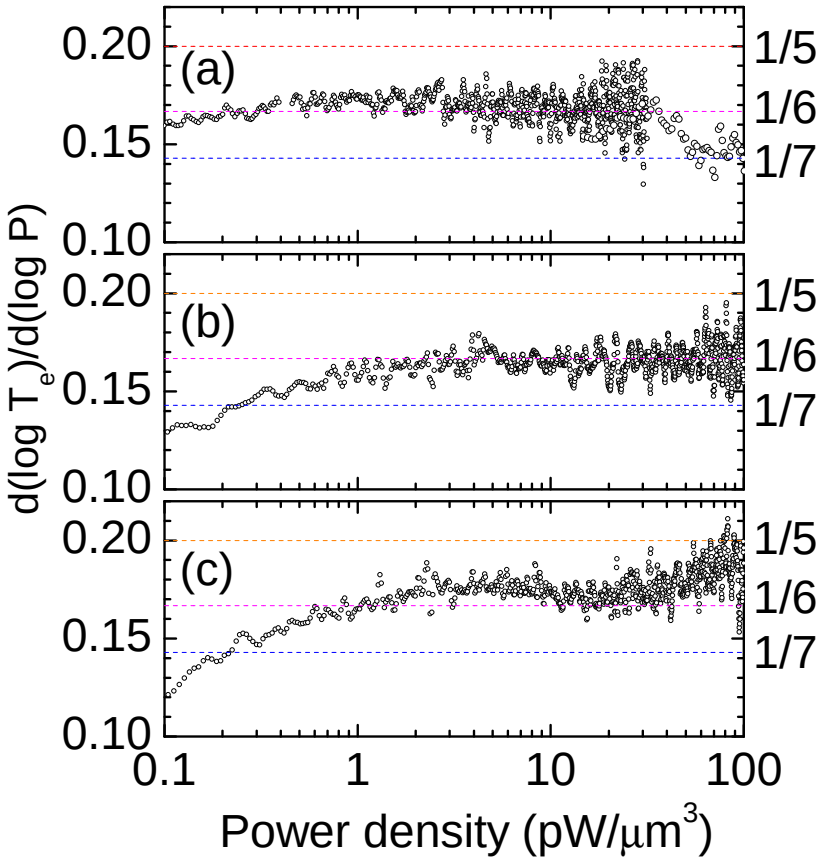

FIGURE 4.6 Numerical logarithmic derivatives of the data in Fig. 4.4: AM2 (a), AM065 (b) and AM03 (c). Dashed lines correspond to 1/5, 1/6, and 1/7 from top down, respectively.

sweeps, which causes the change in the data at about 30 pW/μm^3. For this sample there is an unexplained increase in n at high power densities. In data for AM03 there is again decrease in n approaching the value n = 5 above 10 pW/μm^3. Very similar derivative was seen for the data for CU33 in Section 3.2.2. One can again speculate about possible effect of the Kapitza resistance on the result for this sample, but nothing certain can be said. It is possible that in some samples residues of resist or some other substance could make the thermal resistance between the metal film and the substrate bigger, although extra care was taken to keep the substrate as clean as possible at all stages in sample fabrication.

Measurements show that the electron-phonon interaction in AlMn can be adjusted by changing the Mn concentration, since the electron mean free path changes with c_i. This is interesting from technological point of view. For example for hot-electron bolometers, lowering the e-p coupling leads to an increased sensitivity. Finite thermal conductivity G through which the energy from the electrons relaxes,

produces thermal fluctuations. These will limit the detector performance. Noise equivalent power for the hot-electron bolometer is $\mathrm{NEP} = \sqrt{4k_{\mathrm{B}}T^2G}$ [62]. Thermal conductivity at low temperature is usually dominated by electron-phonon interaction, so $G = 1/R_{\mathrm{e-p}}$, where thermal resistace $R_{\mathrm{e-p}}$ is given by Eq. 3.5. Noise equivalent power can then be written as $\mathrm{NEP} = \sqrt{4k_{\mathrm{B}}T^2n\Sigma\mathcal{V}T^{n-1}}$. The linear dependence of Σ on l suggest as large manganese concentration as possible for the bolometer application. Same goes for the electron coolers, whereas in the applications where the lattice is also to be cooled, Mn concentration should be small. Substantial variation of Σ versus l in Cu films (Chapter 3) could be utilized for tailoring the e-p coupling in the same way.

5 Tunnel junction arrays in weak Coulomb blockade regime

Classically, two conducting electrodes of area A and separation d on top of each other with no electrical contact between them form a capacitor. Capacitance of such a structure is $C = \epsilon_0 \epsilon A/d$, where ϵ is dielectric constant of the insulating material between the electrodes. When one electron of charge *e* is transferred through the barrier from one electrode to the other, the capacitance *C* related to the junction is charged leading to a voltage change $\delta V = e/C$. The energy needed for charging is then $E_{Ch} = e^2/2C$. For small tunnel junctions ($A = 100 \times 100$ nm^2), easily fabricated by standard EBL method, the capacitance will be of the order of 1 fF corresponding to $E_{Ch} \sim 10^{-4}$eV. If R_{T} is bigger than the quantum of resistance ($R_{\mathrm{K}} \sim 25.8$ kΩ), the quantum fluctuations are suppressed. If the temperature is also very low, so that $k_{\mathrm{B}}T \leq E_{\mathrm{Ch}}$ (which gives a typical temperature range T < 1 K), then the electrons are confined in each of the 2 electrodes and *charging effects* may appear. In this situation, one extra electron on junction blocks other electrons from tunneling. This phenomenon is the so-called *Coulomb blockade of tunneling* [11].

Arrays of tunnel junctions can be used for thermometry by making use of the so-called partial Coulomb blockade, i.e. the situation where the charging energy is smaller than the thermal energy. *Electromagnetic environment* of the tunnel junction array will affect the electrical properties and, therefore, the thermometry by the arrays. In this chapter, the basic theory of the Coulomb blockade thermometry is reviewed. Conductance measurements of 1D and 2D tunnel junction arrays are presented. Results for the smallest arrays are compared with the numerical calculations, where electromagnetic environment is modeled with resistance.

5.1 Coulomb blockade thermometry

Coulomb blockade thermometer (CBT) is an array of tunnel junctions. CBT was invented in Jyväskylä more than ten years ago and is a simple absolute thermometer for cryogenic applications [50,24,41]. 2D tunnel junction arrays have been shown to function as thermometers the same way than their 1D counterparts [16,17,22].

CBT can be used in a temperature range where the charging energy $E_{\mathrm{C}} \equiv 2(N-1)/N \times (e^2/2C) \sim k_{\mathrm{B}}T$, i.e., in the partial Coulomb blockade regime (C is

capacitance of a tunnel junction in homogeneous array and N is number of tunnel junctions in the array). The conductance curve of an array can be calculated against $v_{\mathrm{N}} \equiv eV/Nk_{\mathrm{B}}T$ for expansion parameter $u_{\mathrm{N}} \equiv E_{\mathrm{C}}/k_{\mathrm{B}}T$ small enough, utilizing the so-called orthodox theory [11]. The first order result in u_{N} is linear, that is,

$$\frac{G(v)}{G_T} = 1 - u_N g(v_N), \tag{5.1}$$

where G_{T} is conductance of the array at large bias voltages and $g(v) \equiv [v\ \sinh(v) - 4\ \sinh^2(v/2)]/8\ \sinh^4(v/2)$ defines the shape of the conductance curve. The general equation for an inhomogeneous array has been calculated in [33] and it is

$$\frac{G(v)}{G_{\mathrm{T}}} = 1 - 2\sum_{i=1}^{N} \frac{R_{\mathrm{T,i}}}{R_\Sigma} \frac{\Delta_i}{k_{\mathrm{B}}T} g\left(\frac{R_{\mathrm{T,i}}}{R_\Sigma}\frac{eV}{k_{\mathrm{B}}T}\right), \tag{5.2}$$

where $R_\Sigma = \Sigma_{i=1}^{N} R_{\mathrm{T,i}}$ is the total tunnel resistance and $\Delta_i = (C^{-1}_{i-1,i-1} + C^{-1}_{i,i} - 2C_{i,i-1})e^2/2$ is the Coulomb Blockade threshold arising from the inverse capacitance matrix $\mathbf{C^{-1}}$ [37].

The conductance curve exhibits a drop at small transport voltages. The full width at half minimum of the conductance drop for the homogenous array ($R_{\mathrm{T,i}} \equiv R_{\mathrm{T}}$, $C_i \equiv C$ and $C_{o,i} = 0$) calculated from Eq. 5.1 is

$$V_{1/2,0} = 5.439 N k_B T/e. \tag{5.3}$$

Equation 5.3 states, that the full width at half minimum depends only on constants of nature and known parameter N, hence an array of tunnel junctions can be used as a primary thermometer. Known correction for the first order result in linear regime, $\Delta V_{1,2} = V_{1/2} - V_{1/2,0}$, is $\Delta V_{1/2}/V_{1/2,0} \approx 0,39211 \Delta G/G_T$, i.e. at low temperature ($E_{\mathrm{C}} \sim k_{\mathrm{B}}T$) measured half width will be smaller than expected from the first order result.

CBT has also a secondary thermometry mode, since the depth of the Coulomb blockade well depends also on temperature:

$$\frac{\Delta G}{G_{\mathrm{T}}} = \frac{1}{6} u_{\mathrm{N}}. \tag{5.4}$$

Parameters needed for the temperature measurement are shown in Fig. 5.1, where a measured conductance curve of a CBT with 100 junctions per array and 25 arrays in parallel measured at 4.25 K is illustrated. Parallel connection of tunnel junction arrays does not affect the thermometry, but lowers the impedance of the device, making the measurements easier.

In deriving equations 5.1–5.4 the voltage bias is assumed to be perfect. In a real situation the electromagnetic environment of the array will prohibit the potential at the ends of the array to stay constant after tunneling of an electron. This phenomenon will affect the conductance, and the conductance dip will be broad-

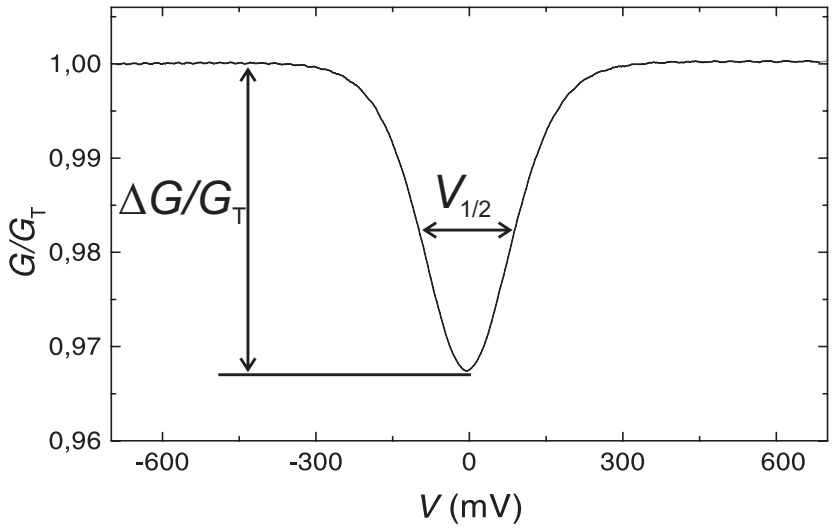

FIGURE 5.1 Measured differential conductance as a function of bias voltage at 4.25 K for a CBT with 100 tunnel junctions in series and 25 arrays in parallel. Quantities yielding the temperature information are drawn in the picture. Full width at half maximum $V_{1/2}$ depends only on the temperature and know constants, enabling primary thermometry. Depth of the conductance dip $\Delta G/G_{\mathrm{T}}$ is proportional to the charging energy and depends inversely on the temperature, and can be used for secondary thermometry.

ened. The effect of electromagnetic environment on tunneling in 1D and 2D tunnel junction arrays will be discussed in more detail in section 5.2. Other sources of error are variations in the tunnel junction resistances in the array [33], strong tunneling ($R_T \leq R_K$) [26] and background charges [24].

5.2 Effect of electromagnetic environment on tunneling

5.2.1 Theoretical background

The effect of the electromagnetic environment on tunneling in tunnel junction arrays can be taken into account by using *phase correlation* theory [37,39,26]. Tunneling rate through a tunnel junction can be calculated from

$$\Gamma_i^{\pm}(\delta F_i^{\pm}) = \frac{1}{e^2 R_{\mathrm{T}}} \int_{-\infty}^{+\infty} \mathrm{d}E \frac{E}{1-\exp[-E/k_{\mathrm{B}}T]} P(-\delta F_i^{\pm} - E), \tag{5.5}$$

where the variable $\delta F_i^{\pm}$ is the change of the free energy when an electron tunnels through the tunnel junction (+ and - define the direction of the tunneling) [37, 25].

Function $P(E)$ is the probability density for an event, where the tunneling electron exchanges energy E with the environment, and reads:

$$P(E) = \frac{1}{2\pi\hbar}\int_{-\infty}^{+\infty} \mathrm{d}t \exp\left[J(t) + \frac{iEt}{\hbar}\right]. \tag{5.6}$$

The electromagnetic environment comes into play through phase-phase-correlation function:

$$J(t) = 2\int_0^{+\infty} \frac{\mathrm{d}\omega}{\omega} \frac{Re[Z_t(\omega)]}{R_K}\left[\coth\left(\frac{\hbar\omega}{2k_BT}\right)[\cos(\omega t) - 1] - i\sin(\omega t)\right], \tag{5.7}$$

where the real part of Z_t, the impedance seen by the tunnel junction, is the essential parameter. Impedance Z_t consists of the capacitance of the tunnel junction itself, capacitance of the other tunnel junctions in the array and the impedance of the environment.

5.2.2 Geometry of the tunnel junction arrays

Tunnel junction arrays were fabricated using standard EBL as described in Section 2.1. Structures used in the measurements are shown in Fig. 5.2. The "aligned" 2D structure can be perceived as a 1D structure with metal islands of the M adjacent arrays connected with tunnel junctions. "Diagonal" structure has M' connections at each busbar and N in this case is the smallest number of tunnel junctions through which busbars are connected, as it is with the "aligned" structure. Smallest 1D structure studied with N, M=2 is denoted **II** and corresponding "aligned" structure **H**. Three different geometries of structures **H** and **II** were fabricated to investigate the influence of the internal structure of an array to the conductance curve. For example, the island length was varied from 1 μm up to 10 μm. Size of the tunnel junctions in all samples was nominally 0.2 $\times$ 0.6 μm^2. Bias voltage was applied at the busbars left and right from the arrays.

5.2.3 Results

Four **II** structures and seven **H** structures were measured at T = 4.25 K, where the linear result for two tunnel junctions in series (Eq. 5.3) predicts $V_{1/2,0}$ = 4.0 mV. Fig. 5.3 shows a typical example of the conductance of a **II** structure and an **H** structure fabricated simultaneously on the same chip. In both cases $\Delta G/G_\mathrm{T} \simeq 0.01$, which implies very small corrections $\Delta V_{1/2}/V_{1/2,0} < 0.4\%$ to the linear result given by Eq. 5.3.

Small but noticeably differences can be seen between the curves in the Fig. 5.3. At first, the dip of the **H** structure is wider than that of the **II** structure. Secondly, the shapes of the dips are not the same; simple scaling of the two curves does not make

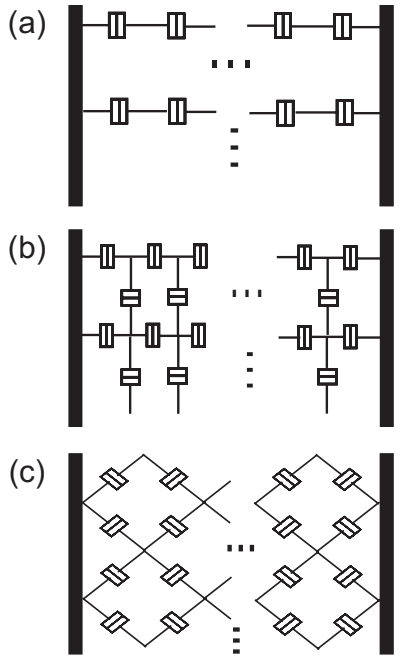

FIGURE 5.2 (a) 1D structure with M parallel arrays each having N tunnel junctions in series, (b) an "aligned" 2D structure, where arrays are connected through tunnel junctions and (c) "diagonal" 2D structure. In "aligned" and "diagonal" structures N is the smallest number of tunnel junctions through which the busbars are connected. Bias voltage was applied to the busbars left and right from the array.

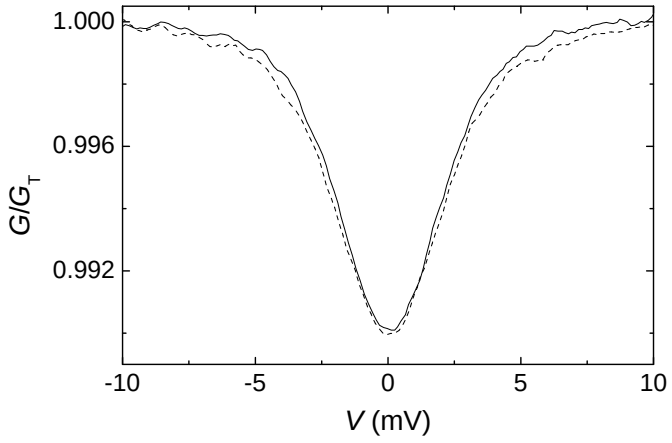

FIGURE 5.3 Differential conductance of **H** (dashed line) and **II** structures as a function of the bias voltage measured at 4.25 K.

them overlap. What is similar in **H** and **II** structures, is that the dips are nearly equally high, when the junction size is the same in **II** and **H**. These facts are not

consistent with the simple sequential tunneling result with zero external impedance.

The main result is that the measured half widths $V_{1/2}$ of the **II** and **H** structures cluster around different values, both higher than $V_{1/2,0}$. For the **II** structure the result was $V_{1/2}$ = 4.53 ± 0.02 mV, and for the **H** $V_{1/2}$ = 4.79 ± 0.05 mV. These results are 13% and 20% larger than the expected from Eq. 5.3. The internal geometry of the arrays did not influence the outcome. This suggests that the corrections to the basic results of Eqs. (5.1)-(5.4) are larger for 2D type structures and are accounted for the electromagnetic environment of the arrays.

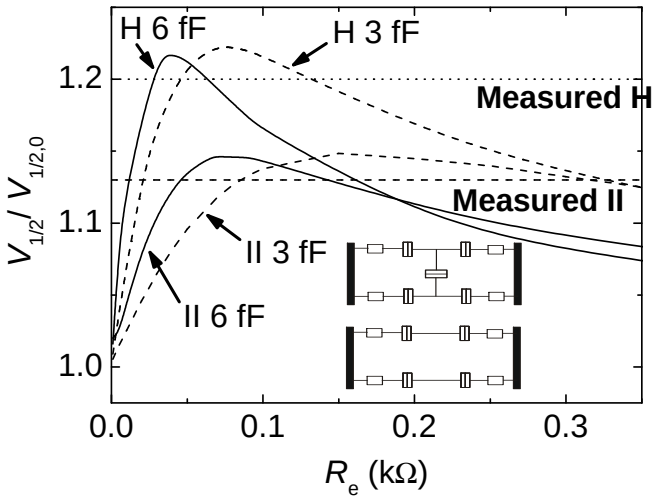

FIGURE 5.4 Calculated half widths normalized to the value given by Eq. 5.3 in **II** and **H** structures as a function of external impedance $R_{\rm e}$. Tunnel junction capacitances used in the calculations were 3 pF and 6 pF. Continuous and dotted horizontal lines are the averages of the measured $V_{1/2}$ for **II** and **H**, respectively. Inset shows the circuit model used in the calculations. Electromagnetic environment is modeled with external resistors $R_{\rm e}$ at the ends of each array.

In the calculation of the current-voltage characteristics **II** and **H** structures, the environment for the arrays was modelled with pure resistive impedance $R_{\rm e}$ as shown in the inset of Fig. 5.4. Curves were obtained by Monte Carlo simulation using an algorithm introduced in [34]. Deduced half widths as a function of external impedance $R_{\rm e}$ for tunnel junction capacitances C = 3 fF and C = 6 fF are shown in Fig. 5.4. Capacitances of the measured tunnel junctions were estimated to be in the range of values used in the calculations.

On-chip impedance is typically a fraction of free space impedance $\sim$ 377 Ω. The value for external impedance in the samples is probably close to the value $R_{\rm e}$, where the maximum of $V_{1/2}$ in the calculations lies for both **II** and **H**. Measured and theoretical values close to maximum values of calculated $V_{1/2}$ agree quite well

even quantitatively: maximum values for **II** and **H** are $V_{1/2}$ = 4.6 mV and 4.9 mV, respectively.

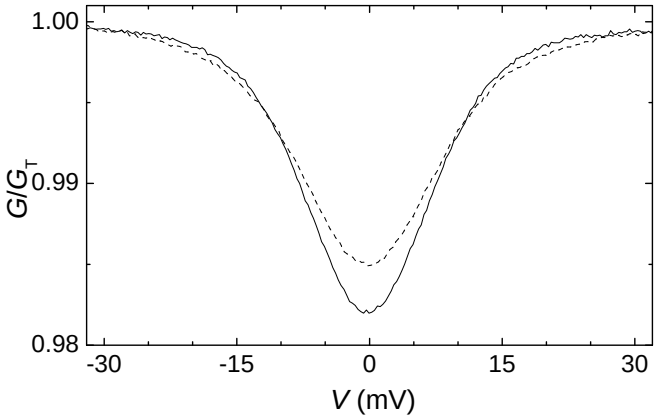

FIGURE 5.5 Measured normalized conductance of an aligned 2D (dashed line) and a 1D array with N = 8 at 4.25 K.

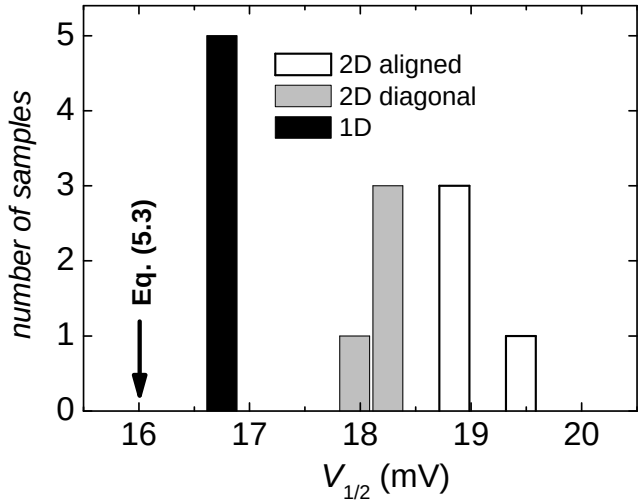

FIGURE 5.6 Histogram of the measured half widths $V_{1/2}$ for the arrays with N = 8. Black pillar represents result for 1D array, grey pillars are for 2D "diagonal" structure and white pillars are for 2D "aligned" structure. Bin size is 0.3 mV.

Several samples with different geometries were measured for the case N = 8. Parallel connections for 1D and aligned 2D had M = 9 and "diagonal" arrays had M'

=4. Fig. 5.5 shows examples of measured conductance curves for a 1D and "aligned" 2D arrays. For N = 8 simple theory predicts $V_{1/2}$ = 16 mV. Histogram of the results is shown in Fig. 5.6. Again, results for 1D arrays are closest to simple theory with $V_{1/2} = 16.68 \pm 0.04$ mV on the average. The "diagonal" 2D arrays have an average half width of $V_{1/2} = 18.20 \pm 0.14$ mV, i.e., it is 14 % wider than the theory would predict. The "aligned" 2D arrays show $V_{1/2} = 19.0 \pm 0.27$ mV, which exceeds $V_{1/2,0}$ by 19 %.

In Fig. 5.7 the ratio of the measured halfwidth $V_{1/2}$ to the simple theory $V_{1/2,0}$ as a function of number of junctions N is plotted. In all the measured sizes, 1D arrays gave $V_{1/2}$ closest to the expected value using Eq. 5.3. The measured half width is approaching the theoretical expectation in both 1D and 2D structures as the number of the tunnel junctions N in the arrays increases. In 1D case this happens faster. Moreover, the scatter of $V_{1/2}$ between similar samples was bigger in 2D structures. This could be related to a stronger sensitivity of $V_{1/2}$ to the value of R_e around the region, where $V_{1/2}$ has maximum value. This is seen for the case N = 2 in Fig. 5.4. As a conclusion, the influence of the external electromagnetic environment on tunneling is stronger for the 2D tunnel junction arrays. This favors the use of 1D structures in thermometry at least when moderate sized arrays are considered.

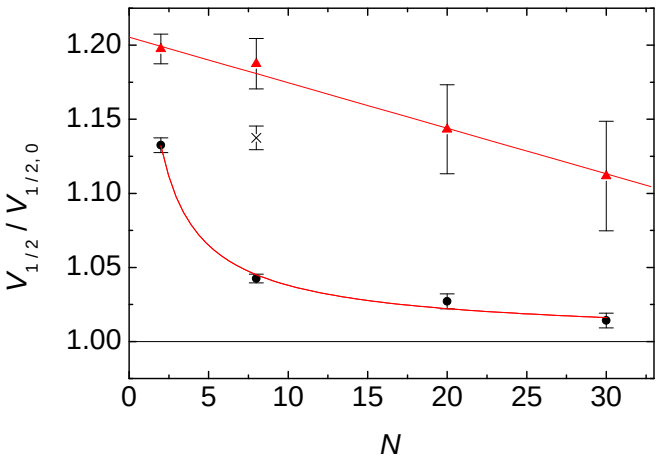

FIGURE 5.7 Half widths $V_{1/2}$ of the conductance curve for 1D (circles), and "aligned" 2D (triangles) structures measured at 4.25 K as a function of N. Result for "diagonal" 2D structure with N = 8 and M' = 4 is shown by a cross. Lines are guides for the eye.

6 Conclusions

Large part of this thesis deals with the electron-phonon interaction in thin metal films. Measurements were based on hot electron effect and sensitive thermometry using normal metal-insulator-superconductor tunnel junctions. Conclusions for noble metal films of gold and copper are, that the power flow between conduction electrons and phonons has a temperature dependence $P_{\mathrm{e-p}} \propto T_{\mathrm{e}}^6 - T_{\mathrm{p}}^6$. This is consistent with the theory for strongly disordered metals, as is the case in the studied films, when electron-phonon scattering of vibrating impurities dominates over the static impurities. This is equivalent with the electron-phonon scattering rate $\tau_{\mathrm{e-p}}^{-1} \propto T_{\mathrm{e}}^4$. However, the electron-phonon coupling constant does not follow the theoretical linear dependence on the electron mean free path l as it should in this case.

Electron-phonon energy relaxation rate in copper was also studied with a method based on ac-heating of the conduction electrons. Due to non-linearity of the electron-phonon interaction, the average temperature of the electrons will increase at heating frequencies larger than the electron-phonon energy relaxation rate. This method was partly developed in this thesis and numerical calculations were performed to verify applicability of the method. Results on energy relaxation rate are partly consistent with the power flow measurements. Temperature dependence of the scattering rate for the thinnest films was in agreement with the dc energy flow measurements. Electron-phonon coupling constant deduced from these measurements differ for two samples with almost same film thickness. This is probably due to different level of disorder in the samples. For the 84 nm thick copper film the temperature dependence of the electron-phonon energy relaxation rate was found to be T_{e}^3, which is expected in the clean limit, in contrast to T_{e}^4 dependence deduced from the dc heating measurement.

Kondo condensate of Aluminum doped with Manganese was studied. Electron-phonon interaction was found to follow the temperature dependence expected for disordered metals. The electron-phonon coupling constant followed roughly linearly the electron mean free path. Resistivity of the films showed a minimum due to the Kondo effect, expected for a metal with magnetic impurities. Low temperature resistivity followed approximately linearly the atomic concentration of manganese in aluminum.

One and two dimensional normal metal tunnel junction arrays were investigated at 4.2 K. Experimental results on partial Coulomb blockade in smallest arrays were compared to Monte Carlo simulations. The outcome was that the 1D arrays

suffered less from the effect of electromagnetic environment on the tunneling than their 2D counterparts. Increasing the number of tunnel junctions in both 1D and 2D arrays lead to a decrease in the deviation from the simple theory based on the orthodox theory.

Bibliography

[1] This thesis article **A.I**.

[2] This thesis article **A.II**.

[3] This thesis article **A.III**.

[4] This thesis article **A.IV**.

[5] This thesis article **A.V**.

[6] This thesis article **A.VI**.

[7] This thesis article **A.VII**.

[8] ALTSHULER, B. L. AND ARONOV, A. G., *Electron-electron interactions in disordered systems*, in *Electron-electron interactions in disordered systems*, edited by A. L. Efros and M. Pollack (Elsevier, Amsterdam, 1985).

[9] ANGHEL, D. V. AND PEKOLA, J. P., *Noise in refrigerating tunnel junctions and in microbolometers*. J. Low. Temp. Phys. **123** (2001) 197–218.

[10] ANTHORE, A., PIERRE, F., POTHIER, H., AND ESTEV, D., *Magnetic-field-dependent quasiparticle energy relaxation in mesoscopic wires*. Phys. Rev. Lett. **90** (2003) 076806.

[11] AVERIN, D. V. AND LIKHAREV, K. K., *Modern problems in condensed matter sciences*, in *Mesoscopic phenomena in solids*, edited by B. L. Altschuler, P. A. Lee, and R. A. Webb (North-Holland, Amsterdam, 1991).

[12] BABIĆ, E., FORD, P. J., RIZZUTO, C., AND SALAMONI, E., *The temperature dependence of the impurity resistivity of AlMn and AlCr*. Solid State Commun. **11** (1972) 519–523.

[13] BABIĆ, E., KRSNIK, R., LEONTIĆ, B., VUČIĆ, Z., ZORIĆ, I., AND RIZZUTO, C., *High-temperature spin-fluctuation resistivity in AlMn*. Phys. Rev. Lett **27** (1971) 805–808.

[14] BARDEEN, J., COOPER, L. N., AND SCHRIEFFER, J. R., *Theory of superconductivity*. Phys. Rev. **108** (1957) 1175–1204.

[15] BÄUERLE, C., MALLET, F., SCHOPFER, F., MAILLY, D., ESKA, G., AND SAMINADAYAR, L., *Experimental test of the numerical renormalization-group theory for inelastic scattering from magnetic impurities*. Phys. Rev. Lett. **95** (2005) 266805.

[16] BERGSTEN, T., CLAESON, T., AND DELSING, P., *Coulomb blockade thermometry using a two-dimensional array of tunnel junctions*. J. Appl. Phys. **86** (1999) 3844–3847.

[17] BERGSTEN, T., CLAESON, T., AND DELSING, P., *A fast, primary Coulomb blockade thermometer*. Appl. Phys. Lett **78** (2001) 1264–1266.

[18] CAPLIN, A. D. AND RIZZUTO, C., *Anomalies in the electrical resistance of Al:Mn and Al:Cr alloys*. Phys. Rev. Lett **21** (1968) 746–748.

[19] CLARK, A. M., MILLER, N. A., WILLIAMS, A., RUGGIERO, S. T., HILTON, G. C., VALE, L. R., BEALL, J. A., IRWIN, K. D., AND ULLOM, J. N., *Cooling of bulk material by electron-tunneling refrigerators*. Appl. Phys. Lett **86** (2005) 173508.

[20] CLARK, A. M., WILLIAMS, A., RUGGIERO, S. T., VAN DEN BERG, M. L., AND ULLOM, J. N., *Practical electron-tunneling refrigerator*. Appl. Phys. Lett. **84** (2004) 625–627.

[21] DEIKER, S. W., DORIESE, W., HILTON, G. C., IRWIN, K. D., RIPPARD, W. H., ULLOM, J. N., VALE, L. R., RUGGIERO, S. T., WILLIAMS, A., AND YOUNG, B. A., *Superconducting transition edge sensor using dilute AlMn alloys*. Appl. Phys. Lett. **85** (2004) 2137–2139.

[22] DEVI, S., BERGSTEN, T., AND DELSING, P., *Experimental test of the correction terms for Coulomb blockade thermometry*. Appl. Phys. Lett **84** (2004) 3633–3635.

[23] DYNES, R. C., GARNO, J. P., HERTEL, G. B., AND ORLANDO, T. P., *Tunneling study of superconductivity near the metal-insulator transition*. Phys. Rev. Lett **53** (1984) 2437–2440.

[24] SH. FARHANGFAR, HIRVI, K. P., KAUPPINEN, J. P., PEKOLA, J. P., TOPPARI, J. J., AVERIN, D. V., AND KOROTKOV, A. N., *One dimensional arrays and solitary tunnel junctions in the weak Coulomb blockade regime: CBT thermometry*. J. Low Temp. Phys. **108** (1997) 191–214.

[25] SH. FARHANGFAR, MANNINEN, A. J., AND PEKOLA, J. P., *Effect of the electromagnetic environment on arrays of small normal metal tunnel junctions: Numerical and experimental investigation*. Europhys. Lett. **49** (2000) 237–243.

[26] SH. FARHANGFAR, POIKOLAINEN, R. S., PEKOLA, J. P., GOLUBEV, D. S., AND ZAIKIN, A. D., *Coulomb blockade in one-dimensional arrays of high-conductance tunnel junctions*. Phys. Rev. B **63** (2001) 075309.

[27] FISHER, P. A., ULLOM, J. N., AND NAHUM, M., *High-power on-chip microrefrigerator based on a normal-metal/insulator/superconductor tunnel junction*. Appl. Phys. Lett **74** (1999) 2705.

[28] GANTMAKHER, V. F., *The experimental study of electron-phonon scattering in metals*. Rep. Prog. Phys **37** (1974) 317–362.

[29] GARST, M., WÖLFLE, P., BORDA, L. ., VON DELFT, J., AND GLAZMAN, L., *Energy resolved inelastic electron scattering off a magnetic impurity*. Phys. Rev. B **72** (2005) 205125.

[30] GERSHENZON, E. M., GERSHENZON, M. E., GOL'TSMAN, G. N., LYUL'KIN, A. M., SEMENOV, A. D., AND SERGEEV, A. V., *Electron-phonon interaction in ultrathin Nb films*. Sov. Phys. JETP **70** (1990) 505–511.

[31] GIAZOTTO, F., HEIKKILÄ, T. T., LUUKANEN, A., SAVIN, A. M., AND PEKOLA, J. P., *Opportunities for mesoscopics in thermometry and refrigeration: Physics and applications*. Rev. Mod. Phys. **78** (2006) 217–274.

[32] HEWSON, A. C., *The Kondo Problem to Heavy Fermions* (Cambridge University press, 1997).

[33] HIRVI, K. P., KAUPPINEN, J. P., KOROTKOV, A. N., PAALANEN, M. A., AND PEKOLA, J. P., *Arrays of normal metal tunnel junctions in weak Coulomb blockade regime*. Appl. Phys. Lett. **67** (1995) 2096–2098.

[34] HIRVI, K. P., PAALANEN, M. A., AND PEKOLA, J. P., *Numerical investigation of one-dimensional tunnel junction arrays at temperatures above the Coulomb blockade regime*. J. Appl. Phys **80** (1996) 256–263.

[35] HUARD, B., ANTHORE, A., BIRGE, N. O., POTHIER, H., AND ESTEVE, D., *Effect of magnetic impurities on energy exhange between electrons*. Phys. Rev. Lett. **95** (2005) 036802.

[36] IL'IN, K. S., PTITSINA, N. G., SERGEEV, A. V., GOL'TSMAN, G. N., GERSHENZON, E. M., KARASIK, B. S., PECHEN, E. V., AND KRASNOSVOBODTSEV, S. I., *Interrelation of resistivity and inelastic electron-phonon scattering rate in impure NbC films*. Phys. Rev. B **57** (1998) 15623–15628.

[37] INGOLD, G.-L. AND YU. V. NAZAROV, *Charge Tunneling Rates in Ultrasmall Junctions*, in *Single charge tunnelling, Coulomb blockade phenomena in nanostructures*, edited by H. Grabert and M. H. Devoret (Plenum, New York, 1992), p. 21.

[38] JOCHUM, J., MEARS, C., GOLWALA, S., SADOULET, B., CASTLE, J. P., CUNNINGHAM, M. F., DRURY, O. B., FRANK, M., LABOV, S. E., LIPSCHULTZ, F. P., NETEL, H., AND NEUHEUSER, B., *Modeling the power flow in normal conductor-insulator-superconductor junctions*. J. Appl. Phys **83** (1998) 3217–3224.

[39] JOYEZ, P. AND ESTEVE, D., *Single-electron tunneling at high temperature*. Phys. Rev. B **56** (1997) 1848–1853.

[40] KAMINSKI, A. AND GLAZMAN, L. I., *Electron energy relaxation in the presence of magnetic impurities*. Phys. Rev. Lett. **86** (2001) 2400–2403.

[41] KAUPPINEN, J. P., LOBERG, K. T., MANNINEN, A. J., PEKOLA, J. P., AND VOUTILAINEN, R. A., *Coulomb blockade thermometer: Tests and instrumentation*. Rev. Sci. Instrum. **69** (1998) 4166–4175.

[42] KIVIOJA, J. M., MAASILTA, I. J., PEKOLA, J. P., AND KARVONEN, J. T., *Response time of a thermometer based on normal metal-insulator-superconductor (NIS) tunnel junction*. Physica E **18** (2003) 21–22.

[43] KONDO, J., *Resistance minimum in dilute magnetic alloys*. Prog. Theor. Phys. **32** (1964) 32–49.

[44] LIDE, D. R. (ed.), *CRC, Handbook of Chemistry and Physics* (CRC press, 1994), 74th ed.

[45] MAKHLIN, Y., SCHÖN, G., AND SHNIRMAN, A., *Quantum-state engineering with Josephson-junction devices*. Rev. Mod. Phys. **73** (2001) 357–400.

[46] NAHUM, M., EILES, T. M., AND MARTINIS, J. M., *Electronic microrefrigerator based on a normal-insulator-superconductor tunnel junction*. Appl. Phys. Lett **65** (1994) 3123–3125.

[47] NAHUM, M. AND MARTINIS, J. M., *Ultrasensitive-hot-electron microbolometer*. Appl. Phys. Lett. **63** (1993) 3075–3077.

[48] PH. NOZIERES AND BLANDIN, A., *Kondo effect in real metals*. J. Physique **41** (1980) 193–211.

[49] PEKOLA, J. P., HEIKKILÄ, T. T., SAVIN, A. M., FLYKTMAN, J. T., GIAZOTTO, F., AND HEKKING, F. W. J., *Limitations in cooling electrons using normal-metal-superconductor tunnel junctions*. Phys. Rev. Lett. **92** (2004) 056804.

[50] PEKOLA, J. P., HIRVI, K. P., KAUPPINEN, J. P., AND PAALANEN, M. A., *Thermometry by arrays of tunnel junctions*. Phys. Rev. Lett **73** (1994) 2903–2906.

[51] PEKOLA, J. P. AND KAUPPINEN, J. P., *Insertable dilution refrigerator for characterization of mesoscopic samples*. Cryogenics **34** (1994) 843–845.

[52] PIERRE, F., ANTHORE, A., POTHIER, H., URBINA, C., AND ESTEVE, D., *Multiple Andreev reflections revealed by the energy distribution of quasiparticles*. Phys. Rev. Lett. **86** (2001) 1078–1081.

[53] PIERRE, F., GOUGAM, A. B., ANTHORE, A., POTHIER, H., ESTEVE, D., AND BIRGE, N. O., *Dephasing of electrons in mesoscopic metal wires*. Phys. Rev. B **68** (2003) 085413.

[54] POTHIER, H., GUÉRON, S., BIRGE, N. O., ESTEVE, D., AND DEVORET, M. H., *Energy distribution function of quasiparticles in mesoscopic wires*. Phys. Rev. Lett. **79** (1997) 3490–3493.

[55] PUTKONEN, M., SAJAVAARA, T., NIINISTÖ, L., AND KEINONEN, J., *Analysis of ALD-prosessed thin films by ion-beam techniques*. Anal. Bioanal. Chem. **382** (2005) 1791–1799.

[56] REIZER, M. Y., *Electron-phonon relaxation in pure metals and superconductors at very low temperatures*. Phys. Rev. B **40** (1989) 5411–5416.

[57] RIZZUTO, C., *Formation of localized moments in metals: experimental bulk properties*. Rep. Prog. Phys. **37** (1974) 147–229.

[58] ROUKES, M. L., FREEMAN, M. R., GERMAIN, R. S., RICHARDSON, R. C., AND KETCHEN, M. B., *Hot electrons and energy transport in metals at millikelvin temperatures*. Phys. Rev. Lett **55** (1985) 422–425.

[59] RUGGIERO, S. T., WILLIAMS, A., RIPPARD, W. H., CLARK, A., DEIKER, S. W., VALE, L. R., AND ULLOM, J. N., *Dilute Al-Mn alloys for low-temperature device applications*. J. Low Temp. Phys. **134** (2004) 973–984.

[60] SAJAVAARA, T., *Heavy ion recoil spectroscopy of surface layers*, Ph.D. thesis, Accelerator Laboratory, Department of Physics, University of Helsinki (2002).

[61] SANTHANAM, P. AND PROBER, D. E., *Inelastic electron scattering mechanisms in clean aluminum films*. Phys. Rev. B **29** (1984) 3733–3736.

[62] SCHMIDT, D. R., LEHNERT, K. W., CLARK, A. M., DUNCAN, W. D., IRWIN, K. D., MILLER, N., AND ULLOM, J. N., *A superconducting-insulator-normal metal bolometer with microwave readout suitable for large-format arrays*. Appl. Phys. Lett. **86** (2005) 053505.

[63] SCHMIDT, D. R., SCHOELKOPF, R. J., AND CLELAND, A. N., *Photon-mediated thermal relaxation of electrons in nanostructures*. Phys. Rev. Lett. **93** (2004) 045901.

[64] SCHMIDT, D. R., YUNG, C. S., AND CLELAND, A. N., *Nanoscale radio-frequency thermometry*. Appl. Phys. Lett **83** (2003) 1002–1004.

[65] SCHMIDT, D. R., YUNG, C. S., AND CLELAND, A. N., *Temporal measurement of hot-electron relaxation in a phonon-cooled metal island*. Phys. Rev. B **69** (2004) 140301.

[66] SERGEEV, A. AND MITIN, V., *Breakdown of Pippard ineffectiviness condition for phonon-electron scattering in micro and nanostructures*. Europhys. Lett. **51** (2000) 641–647.

[67] SERGEEV, A. AND MITIN, V., *Electron-phonon interaction in disordered conductors: Static and vibrating scattering potentials*. Phys. Rev. B **61** (2000) 6041–6047.

[68] SWARTZ, E. T. AND POHL, R. O., *Thermal boundary resistance*. Rev. Mod. Phys **61** (1989) 605–668.

[69] THOMSON, L. F., WILLSON, C. G., AND BOWDEN, M. J. (eds.), *Introduction to microlithography* (American chemical society, 1994), 2nd ed.

[70] TINKHAM, M., *Introduction to superconductivity, 2nd ed.* (McGraw-Hill, New York, 1996).

[71] ULLOM, J. N. AND FISHER, P. A., *Quasiparticle behaviour in tunnel junction refrigerators*. Physica B **284-288** (2000) 2036–2038.

[72] WELLSTOOD, F. C., URBINA, C., AND CLARKE, J., *Hot-electron effects in metals*. Phys. Rev. B **49** (1994) 5942–5956.

[73] ZARAND, G., BORDA, L., VON DELFT, J., AND ANDREI, N., *Theory of inelastic scattering fron magnetic impurities*. Phys. Rev. Lett. **93** (2004) 107204.

[74] ZIMAN, J. M., *Electrons and Phonons* (Oxford, 1960).

[75] ZORIN, A. B., *The Thermocoax cable as the microwave frequency filter for single electron circuits*. Rev. Sci. Instrum. **66** (1995) 4296–4300.